NUMERICAL SIMULATION AND LABORATORY TESTING OF TIME-FREQUENCY MUSIC BEAMFORMING FOR IDENTIFYING CONTINUOUS AND IMPULSIVE GROUND TARGETS FROM A MOBILE AERIAL PLATFORM

A Thesis

by

RAMON ALEJANDRO SILVA

Submitted to the Office of Graduate Studies of
Texas A&M University
in partial fulfillment of the requirements for the degree of

MASTER OF SCIENCE

Approved by:

Chair of Committee,	Yong-Joe Kim
Committee Members,	Luis San Andrés
	Edward White
Head of Department,	Andreas Polycarpou

May 2013

Major Subject: Mechanical Engineering

ABSTRACT

When a microphone array is mounted on a mobile aerial platform, such as an unmanned aerial vehicle (UAV), most existing beamforming methods cannot be used to adequately identify continuous and impulsive ground. Here, numerical simulation results and laboratory experiments are presented that validate a proposed time-frequency beamforming method based on the Multiple Signal Classification (MUSIC) algorithm to detect these acoustic sources from a mobile aerial platform.

In the numerical simulations three parameters were varied to test the proposed algorithm's location estimation performance: 1) the acoustic excitation types; 2) the moving receiver's simulated flight conditions; and 3) the number of acoustic sources. Also, a distance and angle error analysis was done to quantify the proposed algorithm's source location estimation accuracy when considering microphone positioning uncertainty. For experimental validation, three laboratory experiments were conducted. Source location estimations were done for: a 600 Hz sine source, a banded white noise source between 700-800 Hz, and a composite source combined simultaneously with both the sine and banded white noise sources.

The proposed algorithm accurately estimates the simulated monopole's location coordinates no matter the excitation type or simulated trajectory. When considering simultaneously-excited, multiple monopoles at high altitudes, e.g. 50 m, the proposed algorithm had no error when estimating the source's locations. Finally, a distance and angle error analysis exposed how relatively small microphone location error, e.g. 1 cm

maximum error, can propagate into large averaged distance error of about 10 m in the far-field for all monopole excitation types. For all simulations, however, the averaged absolute angle error remained small, e.g. less than 4 degrees, even when considering a 5 cm maximum microphone location error.

For the laboratory experiments, the sine source had averaged distance and absolute angle errors of 0.9 m and 14.07 degrees from the source's true location, respectively. Similarly, the banded white noise source's averaged distance and absolute angle errors were 1.9 m and 47.14 degrees; and lastly, the averaged distance and absolute angle errors of 0.78 m and 8.14 degrees resulted when both the sources were simultaneously excited.

DEDICATION

I dedicate this work to my beloved wife, Juana Gómez Rodríguez, and to my loving parents, María del Refugio Chávez Ortiz and Oscar Silva Sánchez.

ACKNOWLEDGEMENTS

First and foremost, I would like to thank God for bringing me this far in my academic career. Also, I would like to thank my committee chair, Dr. Yong-Joe Kim for all his help and guidance. In addition, I would like to extend my gratitude to Dr. Luis San Andrés and Dr. Edward White for their participation on my defense committee.

In addition, I would like to recognize my colleagues at the Acoustics and Signal Processing Laboratory (ASPL) for all of their help and expertise and, also, the entire faculty and staff in the Mechanical Engineering department here at Texas A&M University. A special thanks goes to the Brazos Valley RC Club (BVRC) members for allowing me to use their airfield and sharing their vast RC knowledge with me.

Finally, I thank all my friends and family for their continuous support; in particular, to my mother and father for their encouragement throughout these years and to my beautiful wife for her ever steadfast patience and love.

NOMENCLATURE

ASPL	Acoustic and Signal Processing Laboratory
B&K	Bruel & Kjær
CIA	Central Intelligence Agency
cRIO	compactRIO
DAQ	Data Acquisition
DFT	Discrete Fourier Transform
DOA	Direction of Arrival
DRAM	Dynamic Random-Access Memory
FPGA	Field-Programmable Gate Array
GPS	Global Positioning System
I/O	Input/Output
LiPo	Lithium-Polymer
LMS	Least Mean Squares
LT	Laboratory Test
LVTTL	Low Voltage Transistor-Transistor Logic
MB	Megabyte
MUSIC	Multiple Signal Classification
NI	National Instrument
NRO	National Reconnaissance Office
RADAR	Radio Detection and Ranging

RC	Remote Controlled
RT	Real-Time
SONAR	Sound Navigation and Ranging
SPL	Sound Pressure Level
SVD	Singular Value Decomposition
UAV	Unmanned Aerial Vehicle
UGS	Unattended ground sensors
WWI	World War I
WWII	World War II

TABLE OF CONTENTS

LIST OF FIGURES

LIST OF TABLES

1. INTRODUCTION AND BACKGROUND

When a microphone array is mounted on a mobile aerial platform, such as an unmanned aerial vehicle (UAV), most existing beamforming methods cannot be used to adequately identify continuous and impulsive ground sources. In this work, an improved time-frequency beamforming method based on the Multiple Signal Classification (MUSIC) algorithm is proposed. The objective of this thesis is to validate the proposed algorithm with: (i) numerical simulations and (ii) laboratory experiments.

In this chapter a concise introduction is given on: early acoustic arrays and UAVs in the battlefield, array signal processing techniques, and current sound source localization literature using aerial acoustic sensor arrays.

1.1 Early acoustic sensor arrays and UAVs in the battlefield

The presence of acoustic sensor technology, during a time of war, dates back to World War I (WWI) where French, Italian, Swedish, and Russian scientists all developed very large ground-based microphone arrays to detect land-based enemy artillery. These early ground-based acoustic arrays consisted of one or two sensor clusters each containing a handful of microphones. Each cluster was rotated along different directions and the output from each microphone was summed. The direction that yielded the maximum total output was taken as the direction of the enemy's artillery. By World War II (WWII), this same technology was aiding in air defense applications to locate and identify aerial threats.[1]

The earliest record of UAV-type applications, in military combat, **dates** back to when old battle-worn B17 and B24 bomber planes were automatically piloted and laden with explosives during WWII.[2] It was in the 1960's when the United States Air Force began operating UAVs for the National Reconnaissance Office (NRO). The UAV's visual reconnaissance capabilities caught the eye of the Central Intelligence Agency (CIA) which later provided most of the funds for UAV research. Although UAV technology has mainly developed for military intelligence and combat needs; much of this drone technology is used in many non-militant applications. Some of these applications include: agricultural crop monitoring, environmental control and weather research, mineral exploration, telecommunications and news broadcasting, and finally, air/ground traffic control.[3]

1.2 Array signal processing

Coming out of WWII, it was clear that having the capability to detect, locate and identify acoustic sources, either man-made or environmental in origin, using sensor arrays or sensor networks was advantageous for numerous monitoring and surveillance applications.[4] As applications expanded, estimation problems to accurately identify temporal and spatial parameters of acoustic sources also gained significant interest. This created the research field we now refer to array signal processing.

One noticeable technique that emerged from this new field of array signal processing is known as *beamforming*. Beamforming was the initial attempt to automatically locate signal sources using spatial filtering at a receiver end. The term *beamforming* derives from the fact that early spatial filters were designed to form pencil beams in order to receive a signal radiating from a specific location and attenuate signals from other locations. Essentially, beamforming "steers" the sensor array over a designated scanning area and measures the output power. The steering locations yielding local maximum power denote the direction of arrival (DOA) estimates. When temporal filtering cannot be used to separate the signal from interference, spatial filtering can exploit the fact that the desired signal and interfering signal usually originate from different spatial locations.[5] As a result, advancements in RADAR, SONAR, communication, imaging, geophysical exploration, and astrophysical exploration have been achieved.[6] One can find numerous works that aim to improve and optimize the standard beamforming technique.

Tremendous interest was again sparked for spectral-analysis-based beamforming methods with the development of the Multiple Signal Classification (MUSIC) algorithm.[7,8] The originality of this MUSIC algorithm was groundbreaking since the MUSIC algorithm explicitly invoked the covariance matrix's eigen-structure, and its intrinsic properties, to provide solutions to the estimation problems. Since MUSIC provided statistically consistent estimates, compared to conventional beamforming; the MUSIC estimator became an alternative to most existing methods; however, MUSIC failed to produce accurate estimates for closely spaced signals in small samples at low

signal-to-noise ratio (SNR). In light of these shortcomings, numerous research groups have proposed a multitude of modifications in attempts to increase the algorithm's efficiency and robustness.[5]

1.3 Acoustic sensor arrays on a mobile aerial platform

Acoustic sensor systems such as SONAR and RADAR continue to be one of the key tools used in twenty-first century battlefields, offering broad battlefield awareness, while being inexpensive, consuming little power, easily transported, and easily camouflaged.

Throughout the twentieth century, acoustic array sensor technologies have emerged to detect and track multiple, impulsive and continuous targets such as gun shots, enemy battle tanks, airplanes, and submarines based on measurements of acoustic pressures radiated from these targets. However, current state-of-the-art technologies are limited to acoustic array measurements made mostly from stationary locations. Recently, much attention has been focused on placing acoustic sensors on mobile platforms such as UAVs and ground vehicles. Placing acoustic array sensors on a mobile aerial platform offers two significant advantages over conventional land-bound platforms: (i) aerial acoustic sensor systems increase the detection range capability per sensor unit, and (ii) aerial acoustic sensor systems can also be less sensitive to the topography of scanned area or to any acoustic reflection from reflective surfaces such as building walls.

Nevertheless, placing acoustic sensors on mobile aerial platforms also provide some technical challenges comprised by high-level platform noise and air flow noise.

Due to these challenges, conventional array signal processing techniques, such as the beamforming method, cannot adequately identify these continuous and impulsive acoustic targets from a UAV.

In the mid-1990's, research groups have again focused on source estimation and localization of aerial and terrestrial impulsive and continuous acoustic targets using single system or networks of unattended ground sensor (UGS) array.[9-12] With attention now on lighter, more mobile, aerial platforms, aerostats equipped with acoustic sensor arrays have been used to detect, localize and classify impulsive and continuous acoustic sources.[13-15] While source detection is accomplished from these stationary aerial sensor arrays, air flow noise and array platform stability were found to be the main contributors to the solution error. In 2007 Robertson and Pham detected the general direction of arrival (DOA) for "periodically-repeated" explosions using a four-element microphone array on a small UAV circling the impulsive source during flight. Robertson and Pham used specially designed microphones in their array that mechanically filtered flow noise. In order to mitigate the platform noise from the measured impulsive source data, least mean squares (LMS) adaptive filtering and match filtering was used.[16-17]

In this proposed work, a numerically simulated moving aerial platform (i.e. UAV) is flown across an open airfield with multiple impulsive and continuous acoustic sources at ground-level. Contrary to Robertson and Pham's work[16], the impulsive source behaves as a transient source with no periodically-repeated impulsive event. To detect these acoustic sources an improved time-frequency MUSIC beamforming algorithm is proposed. With this proposed algorithm the acoustic source's relative location, with

respect to the moving platform, is obtained in addition to the DOA. Laboratory tests are also performed to further validate the proposed algorithm.

2. THEORY

In this chapter, the sound pressure field equation for a stationary monopole, a stationary medium and a moving receiver is derived. This sound pressure field equation is used in the numerical simulations. Also, the proposed time-frequency MUSIC beamforming algorithm is explained.

2.1 Sound pressure field: stationary monopole, stationary medium and moving receiver

Although experimental cases comprise of stationary sources, a stationary medium, and a moving receiver (i.e., a UAV), the equivalent system with moving monopole sources, a moving medium, and a stationary receiver is considered here to analytically represent the sound pressure fields radiated from monopoles and then measured on a UAV. This equivalent system for a single monopole case can be seen in Fig. 2.1.

As mentioned in the experimental case, the monopole source, at point *S*, is stationary with respect to the fluid medium at position $\mathbf{r}_s$ with coordinates x_s, y_s, and z_s. The moving receiver's path is specified by vector $\mathbf{r}(t)$ with components $x(t)$, $y(t)$, and $z(t)$, at point *D*, and travels at a constant velocity *V* in the positive x-direction. Also, note that the sound pressure observed by $\mathbf{r}$ at time t was emitted by the source at time τ, at point *E*. Similarly, in the analytical case, the moving monopole's path is specified by vector $\mathbf{r}_s(t)$ with component $x_s(t)$, $y_s(t)$, and $z_s(t)$, at point *S*. Both the monopole source

and the fluid medium travels at a constant velocity V in the negative x-direction. The stationary receiver is at position **r** with coordinates x, y, and z. Similar to the experimental case the sound pressure observed by **r** at time t was emitted by the source at time τ, at point E.

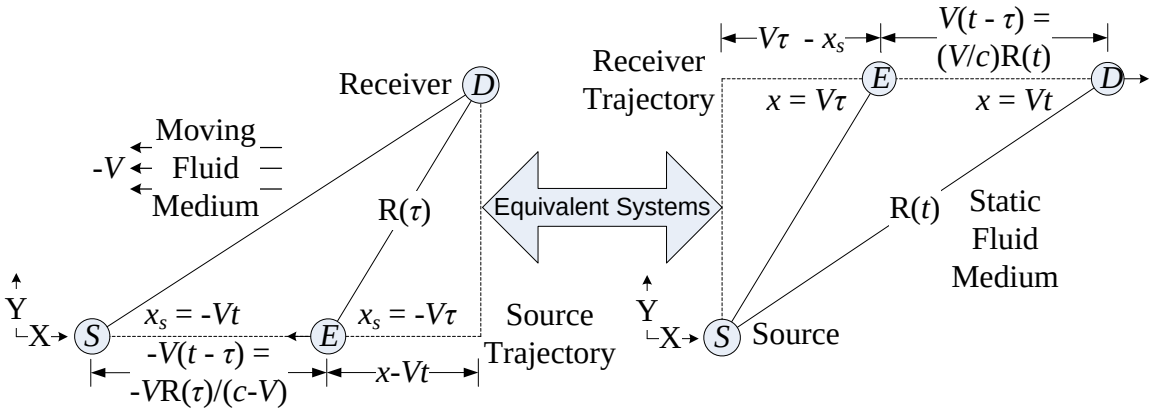

Figure 2.1. Monopole, medium and receiver equivalent systems

The inhomogeneous convective wave equation for the described equivalent system can be written in terms of the acoustic velocity potential, $\phi(x, y, z, t)$ in the stationary receiver's coordinate system, as

$$\nabla^2\phi - \frac{1}{c^2}\frac{D^2\phi}{Dt^2} = -q(t)\delta(x+Vt)\delta(y)\delta(z)\,; \tag{2.1}$$

where q is the monopole strength that represents the total rate of mass flux out of the monopole source, V is the velocity of the monopole source and the moving medium, lastly, D/Dt denotes the total derivative defined as

$$\frac{D}{Dt} = \frac{\partial}{\partial t} - V\frac{\partial}{\partial x}\,. \tag{2.2}$$

After solving Eq. 2.1 for the velocity potential Eq. 2.3 is used to describe the proposed system's corresponding sound pressure field.

$$p = \frac{D\phi}{Dt} = (\frac{\partial}{\partial t} - V\frac{\partial}{\partial x})\phi\,. \tag{2.3}$$

In attempts to transform Eq. 2.1 into a simpler wave equation that represents the radiation from a stationary source to a stationary receiver, the Prandtl-Glauert[18] transformation is used. First define the coordinate transformation,

$$\chi = \frac{x}{\beta},\ T = \beta t - \frac{M\chi}{c},\ \psi = y,\ \zeta = z \tag{2.4}$$

with constants

$$M = \frac{V}{c},\ \beta = \sqrt{1-M^2},\ \gamma = \frac{1}{\beta}\,. \tag{2.5}$$

In Eq. 2.5, c is the speed of sound in air and the monopole source is assumed to travel only at subsonic velocities, i.e., the Mach number $M = V/c < 1$. Using the coordinate transformations in Eq. 2.4, the first order and second order partial-derivatives become:

$$\frac{\partial}{\partial x} = \frac{\partial\chi}{\partial x}\frac{\partial}{\partial\chi} + \frac{\partial T}{\partial x}\frac{\partial}{\partial T} = \frac{1}{\beta}\frac{\partial}{\partial\chi} - \frac{M}{c\beta}\frac{\partial}{\partial T}$$

$$\frac{\partial}{\partial t} = \frac{\partial\chi}{\partial t}\frac{\partial}{\partial\chi} + \frac{\partial T}{\partial t}\frac{\partial}{\partial T} = \beta\frac{\partial}{\partial T}$$

$$\frac{\partial^2}{\partial x^2} = \frac{\partial}{\partial x}(\frac{\partial}{\partial x}) = \frac{1}{\beta^2}\frac{\partial^2}{\partial\chi^2} - \frac{2M}{c\beta^2}\frac{\partial^2}{\partial T\partial\chi} + \frac{M^2}{c^2\beta^2}\frac{\partial^2}{\partial T^2} \tag{2.6}$$

$$\frac{\partial^2}{\partial t^2} = \frac{\partial}{\partial t}(\frac{\partial}{\partial t}) = \beta^2\frac{\partial^2}{\partial T^2}$$

$$\frac{\partial^2}{\partial t\partial x} = \frac{\partial}{\partial t}(\frac{\partial}{\partial x}) = \frac{\partial^2}{\partial T\partial\chi} - \frac{M}{c}\frac{\partial^2}{\partial T^2}\,.$$

After applying all the substitutions, Eq. 2.1 is written as

$$(\frac{\partial^2}{\partial\chi^2}+\frac{\partial^2}{\partial\psi^2}+\frac{\partial^2}{\partial\zeta^2})\Phi-\frac{1}{c^2}\frac{\partial^2\Phi}{\partial T^2}=-q(\gamma(T+\frac{V\chi}{c^2}))\delta(\gamma(\chi+VT))\delta(\psi)\delta(\zeta)\,. \quad (2.7)$$

Note that the Prandtl-Glauert transformation simplifies the problem to a stationary receiver and moving source case. Applying the Lorentz Transformation,[19] as shown below,

$$\chi'=\gamma(\chi+VT),\ T'=\gamma(T+\frac{V\chi}{c^2}),\ \psi'=\psi,\ \zeta'=\zeta \quad (2.8)$$

to Eq. 2.7 again simplifies the wave equation to

$$(\frac{\partial^2}{\partial\chi'^2}+\frac{\partial^2}{\partial\psi'^2}+\frac{\partial^2}{\partial\zeta'^2})\Phi'-\frac{1}{c^2}\frac{\partial^2\Phi'}{\partial T'^2}=-q(T')\delta(\chi')\delta(\psi')\delta(\zeta')\,. \quad (2.9)$$

Eq. 2.9 gives us a inhomogeneous wave equation analogous to one representing the radiation from a stationary source with strength *q(T')*. The solution to Eq. 2.9 can be expressed directly in terms of coordinates *r'* and *T'*.

$$\Phi'(r',T')=\frac{q[\tau']}{4\pi r'} \quad \text{where} \quad \tau'=T'\mp\frac{r'}{c} \quad (2.10)$$

In Eq. 2.10, τ' is defined at the retarded time in the prime coordinate system. Retarded time gives the time when the moving source first emitted the signal. Transforming Eq. 2.10 back to the initial coordinate system (*x, y, z, t*);

$$\tau'=T'\mp\frac{r'}{c}=\gamma(T+\frac{V\chi}{c^2})\mp\frac{1}{c}\sqrt{\chi'^2+\psi'^2+\zeta'^2}=\gamma(T+\frac{V\chi}{c^2})\mp\frac{1}{c}\sqrt{(\gamma(\chi+VT))^2+\psi^2+\zeta^2}$$

$$\tau=t-\frac{R_1}{c} \quad \text{where} \quad R_1=\sqrt{(x+Vt)^2+y^2+z^2}\,,$$

The velocity potential ϕ becomes

$$\phi(x,y,z,t) = \frac{q[(t-\frac{R_1}{c})]}{4\pi R_1} \ . \tag{2.11}$$

Using the relationship expressed in Eq. 2.3, the sound pressure field is expressed as

$$p(x,y,z,t) = \frac{\partial}{\partial t}(\frac{q[(t-\frac{R_1}{c})]}{4\pi R_1}) - V\frac{\partial}{\partial x}(\frac{q[(t-\frac{R_1}{c})]}{4\pi R_1}) \ . \tag{2.12}$$

By implementing the chain rule and the simplifications, the sound pressure field becomes

$$p(x,y,z,t) = \frac{\frac{\partial q}{\partial \tau}[(t-\frac{R_1}{c})]}{4\pi R_1}. \tag{2.13}$$

2.2 Time-frequency MUSIC beamforming

The time-frequency MUSIC beamforming approach utilizes both temporal and spectral information to effectively identify transient acoustic sources. This algorithm uses the averaged spectral (or frequency) data obtained by applying a discrete Fourier transform (DFT) to the windowed temporal (or time) data, at a specific time, collected by the microphone array on the moving platform flying over the continuous and impulsive acoustic sources.[20] The current method is a post processing procedure; however, this method can be adapted for a real-time processing.

Consider $x_m(t)$ to represent sound pressure data measured by the m^{th} microphone of an array and sampled at frequency f_s, where t denotes time. From Fig. 2.2, a cluster of

N data points, $x_m(t_n)$, centered at time step t_n is extracted from $x_m(t)$ to create an $M \times M$ averaged cross-spectral matrix, $\mathbf{R}_{\text{avg},n}(t_n,f)$, where M is the number of microphones.

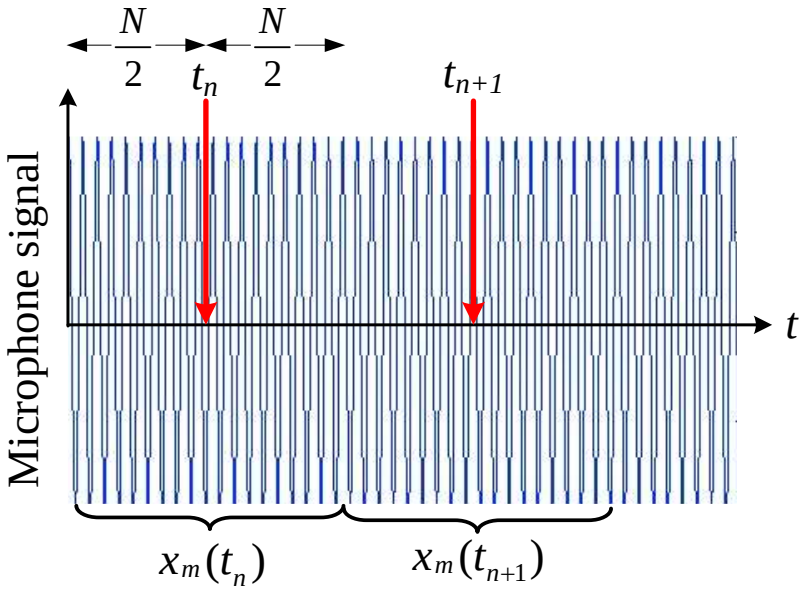

Figure 2.2. Extraction of N data points centered at time step t_n.

Fig. 2.3 shows a Hanning window, w_1 with length D, applied to $x_m(t_n)$, starting from $\tau_1 = t_n - (N/2)\cdot(1/f_s)$, where D must be smaller than N. A Hanning window is applied in attempts to mitigate truncation noise. While keeping its indexed location, the windowed data is then inserted into a zero vector of length L ($L > N$) to increase spectral resolution. Then, a cross spectral matrix (CSM), $\mathbf{R}_1(t_n,f)$, is obtained at each frequency by applying the DFT to these windowed temporal data, of length L. After calculating $\mathbf{R}_1(t_n,f)$, the Hanning window is moved to start at time step τ_2, using Eq. 2.14, and reapplied to $x_m(t_n)$ to calculate $\mathbf{R}_2(t_n,f)$.

$$\tau_{j+1} = \tau_j + \frac{1}{4}\frac{D}{f_s} \tag{2.14}$$

In Eq. 2.14, it is assumed that the data is overlapped by 75 % for calculating the averaged CSM. Each succeeding CSM is added to the previous at each frequency. This sequence continues until the J^{th} iteration when all points within $x_m(t_n)$ have been windowed.

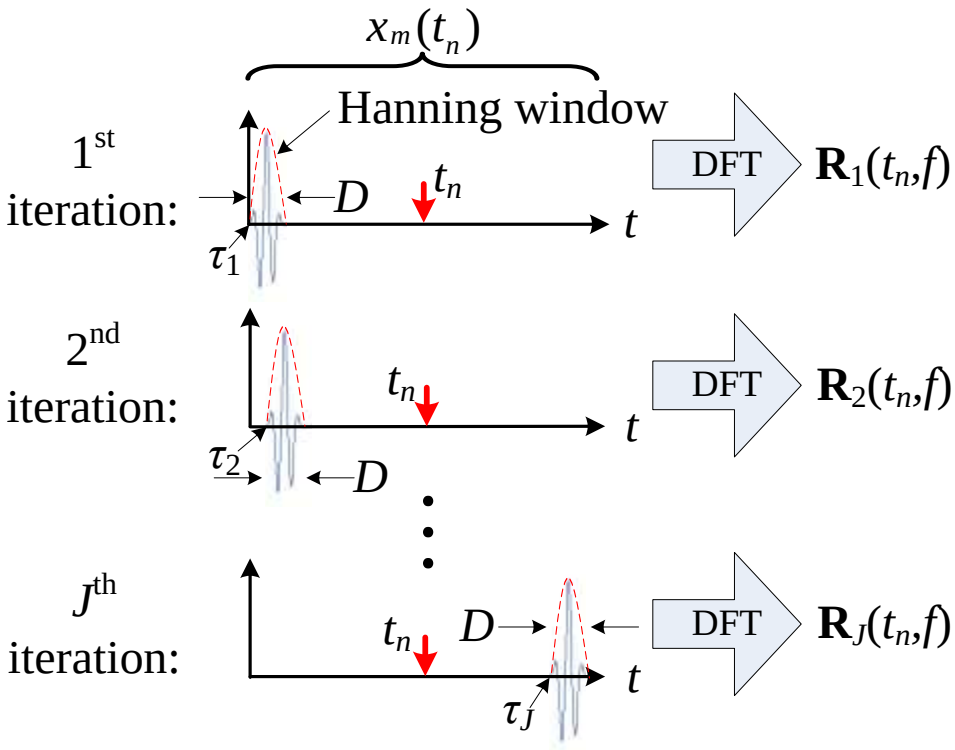

Figure 2.3. Cross-spectral matrix calculation at time step t_n.

When considering a general time step t_n and j^{th} iteration, Eq. 2.15 can be used to calculate the CSM.

$$\mathbf{R}_j(t_n, f) = \mathbf{X}_j(t_n, f) \cdot \mathbf{X}_j^{\mathrm{H}}(t_n, f) \tag{2.15}$$

where

$$\mathbf{X}_j(t_n, f) = [\tilde{x}_1(t_n, f)\ \ \tilde{x}_2(t_n, f)\ \tilde{x}_3(t_n, f) \cdots \tilde{x}_M(t_n, f)]^T \tag{2.16}$$

$$\tilde{x}_m(t_n, f) = \mathrm{DFT}[w_j \cdot x_m(t_n)]. \tag{2.17}$$

Finally, the averaged cross-spectral matrix is calculated at each frequency using

$$\mathbf{R}_{avg,n}(t_n, f) = \frac{1}{J}\sum_{j=1}^{J}\mathbf{R}_j(t_n, f). \tag{2.18}$$

Then, the singular value decomposition (SVD) is applied to the averaged cross-spectral matrix in Eq. 2.18, i.e.,

$$\mathbf{R}_{avg,n}(t_n, f) = \mathbf{U}(t_n, f)\mathbf{\Sigma}(t_n, f)\mathbf{V}^{\mathrm{H}}(t_n, f) \tag{2.19}$$

which is then used to calculate the time-frequency MUSIC power at each scanning point, as seen below.[18]

$$P_{\mathrm{MUSIC},n}(t_n, f, \mathbf{r}_s) = \frac{1}{\sum_{m=p+1}^{M}\left|\mathbf{g}^{\mathrm{H}}(\mathbf{r}_s)\cdot\mathbf{u}_m(t_n, f)\right|^2} \tag{2.20}$$

In Eq. 2.20, $\mathbf{g}$ and $\mathbf{r}_s$ is the spherical wave scanning vector and the scanning location vector of length Q, respectively.

$$\mathbf{g} = \frac{e^{-ik\mathbf{r}_s}}{\mathbf{r}_s} \tag{2.21}$$

$$\mathbf{r}_s(x_s, y_s, z_s) = [r_1(x_s, y_s, z_s)\ \ r_2(x_s, y_s, z_s)\cdots r_Q(x_s, y_s, z_s)]^T \tag{2.22}$$

Also, the noise subspace basis vector, $\mathbf{u}_m$, is the m^{th} column vector from matrix $\mathbf{U}(t_n,f)$ in Eq. 2.19 and p is the dimension of the signal space. When the scanning location coincides with the source location, the inner product in the denominator in Eq. 2.20 becomes a small value since both vectors are orthogonal to each other; thus, the MUSIC

power is locally maximized at the particular scanning location. This cycle repeats until all time points within $x_m(t)$, $m = 1, 2, \ldots, M$, are processed.

3. FLIGHT TEST SIMULATIONS

In this chapter the simulated flight test setup, processing procedure and results are presented. In order to test the proposed algorithm's performance, three parameters were studied: (1) the acoustic excitation type, i.e., tonal excitation, banded white noise excitation, and impulse excitation; (2) the moving receiver's simulated flight conditions, e.g., velocity, altitude and flight trajectory; and (3) the number of acoustic sources. Also, a distance error and angle error analysis is done to quantify the proposed algorithm's source location estimation accuracy when considering microphone location uncertainty.

3.1 Simulated flight test setup

A simulated mobile aerial receiver contains an array of 7 microphones placed at the microphone coordinates (x_m, y_m, z_m) expressed in Figure 3.1, relative to the UAV's coordinate origin. This moving receiver is given a particular set of simulated flight conditions, i.e. velocity, altitude and flight trajectory, to traverse a designated area containing simulated impulsive and continuous monopole sources, as shown in Fig. 3.2.

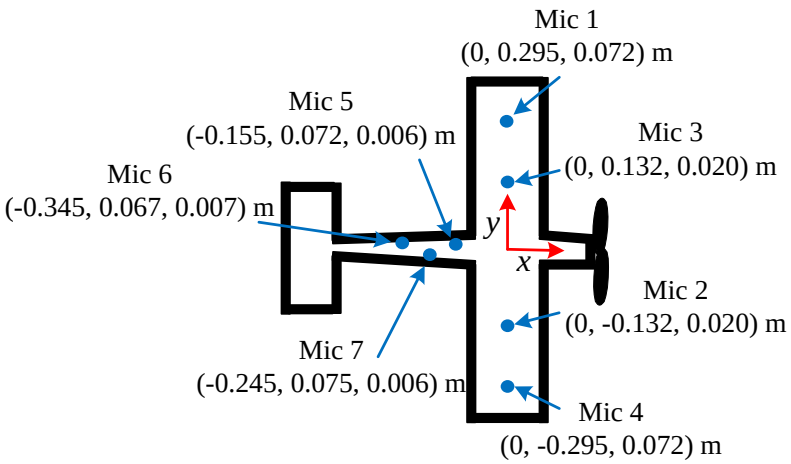

Figure 3.1 Top view of the array microphone locations for the simulated flight tests.

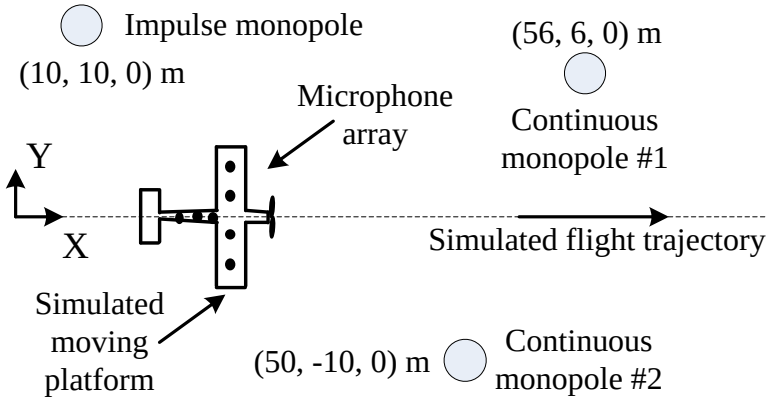

Fig 3.2. Simulated flight configuration.

3.2 Simulated flight test processing procedure

For the flight test simulations: the sampling frequency, $f_{s,}$ is 3.657 kHz; the initial time step, $t_{1,}$ is 128 / f_s = 0.035 seconds; the extracted data length, N, is 256 data points; the Hanning window length, D, is 32 data points; and the zero vector length, L, is 1024

data points. Please refer to section 2.2 in this report for more information about the proposed processing procedure.

Let $\mathbf{x}(t_1)$ define a time block of 7 × 256 data points extracted from the total sound pressure field data centered at t_1 = 0.035 seconds. While maintaining its indexed locations, a Hanning-windowed 7 × 32 section of $\mathbf{x}(t_1)$, starting at τ_1 = 0 seconds, is extracted and placed into a 7 × 1024 zero matrix. Then, an instantaneous 7 × 7 CSM is calculated for each frequency. The 7 × 32 Hanning window is then moved to start at τ_2 = 0.002 seconds and reapplied to $\mathbf{x}(t_1)$. This second set of windowed data is also placed into another 7 × 1024 zero matrix and an instantaneous 7 × 7 CSM is calculated for each frequency. Each CSM is added the previous until all the point within $\mathbf{x}(t_1)$ have been windowed. Then, the $\mathbf{R}_{\text{avg},1}(t_1,f)$ is calculated and SVD is applied. Using Eq. 2.20 the time-frequency MUSIC power is calculated at each scanning point of the designated scanning area. The scanning area is a 40 × 40 grid spanning (X,Y) = ([0,78],[-40,38]) m with ΔX = ΔY = 2 m. This process repeats at the next time step until all 4 seconds of sound pressure field data is processed.

3.3 Simulated flight test results

3.3.1 Effects of acoustic excitation

In this study three different monopole excitation types were used: a 600 Hz tonal source; a banded white noise source between 700-800 Hz; and an impulse source. Each source was excited individually. Each source's location coordinates, sound pressure level (SPL) at 1 m, duration and delay before triggering can be seen in Table 3.1.

Table 3.1. Acoustic source excitation parameters.

Excitation	Location (X_s, Y_s, Z_s) [m]	SPL at 1 m [dB/20μPa]	Duration [sec]	Delay from t = 0* [sec]
Sine (600 Hz)	(56, 6, 0)	95	4	N/A
Banded white noise (700-800 Hz)	(50, -10, 0)	95	4	N/A
Impulse	(10, 10, 0)	95	0.005	0.1

*The simulated mobile platform is at the (X,Y) = (0,0) at t = 0.

Also, the simulated moving receiver takes the y = 0 line as its flight trajectory and travels at a constant 17.5 m/s velocity, solely in the positive x-direction, with a constant 50 m altitude, as seen in Fig. 3.3, in each excitation study mentioned.

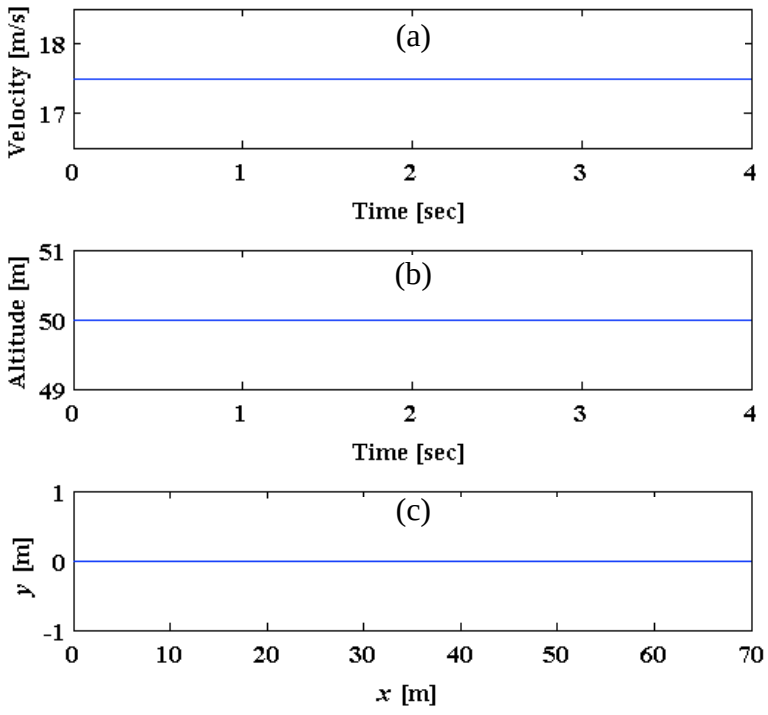

Figure 3.3. Simulated moving receiver with constant velocity, altitude, and trajectory: (a) velocity, (b) altitude, and (c) trajectory.

Fig. 3.4 and Fig. 3.5 show the normalized MUSIC power maps on the scanning area at the 1.08 sec time step with the tonal excitation and the banded white noise excitation, respectively. Fig. 3.6 shows the normalized MUSIC power map of the scanning area at the 0.24 sec time step with the impulse excitation. On each normalized MUSIC power map the "+" denotes the UAV's position at each time step, the "o" shows the impulse source's location and the "x" gives the coordinates for the continuous sources. These MUSIC power maps are calculated using the averaged cross-spectral matrices, scanning vector and scanning locations outlined in section 2.2. For Fig. 3.4 – Fig. 3.6, only the frequencies of concern where considered to plot the MUSIC power; e.g., only the 600 Hz frequency was considered when estimating the 600 Hz monopole's location. Likewise, only the frequencies between 700 Hz and 800 Hz were considered when estimating the banded white noise monopole's location. The maximum MUSIC power location estimation in Fig. 3.4 - Fig. 3.6 always coincides with each source's true location coordinates; thus, each source location is properly estimated.

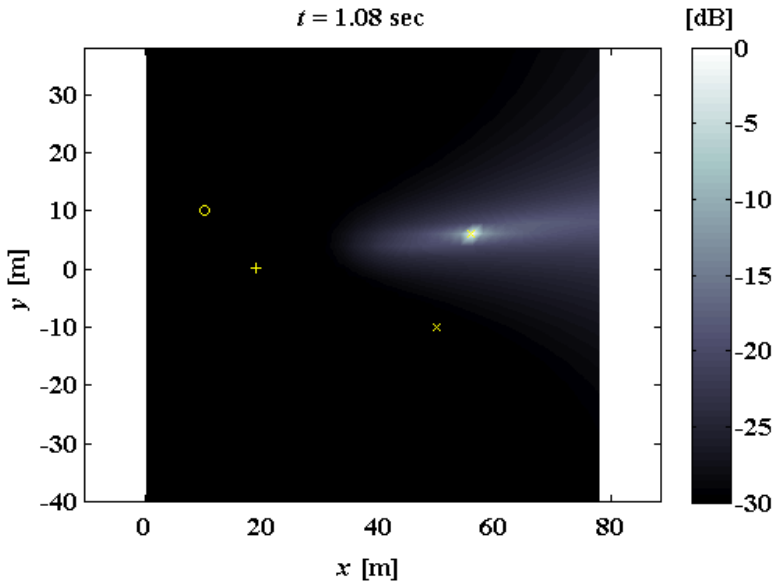

Figure 3.4. Normalized MUSIC power map at t = 1.08 sec estimating the monopole's location with tonal excitation.

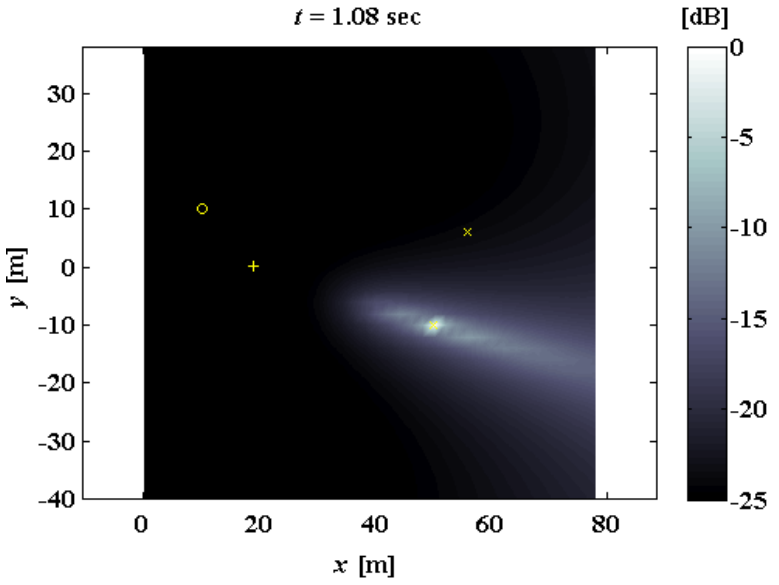

Figure 3.5. Normalized MUSIC power map at t = 1.08 sec estimating the monopole's location with banded white noise excitation.

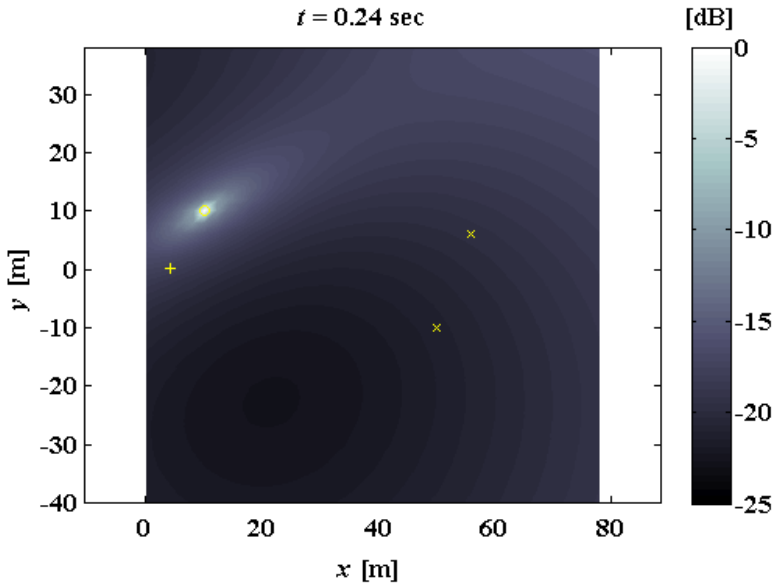

Figure 3.6. Normalized MUSIC power map at *t* = 0.24 sec estimating the monopole's location with impulse excitation.

3.3.2 Effects of simulated flight condition

In this study the same three sources described in Table 3.1 are reused; however, the simulated moving receiver's velocity, altitude and trajectory are determined by the GPS information collected in the proposed UAV during one of the preliminary flight tests. The proposed UAV and flight test configuration are later explained. Fig. 3.7 shows the velocity, altitude and flight trajectory information collected from the GPS data logger.

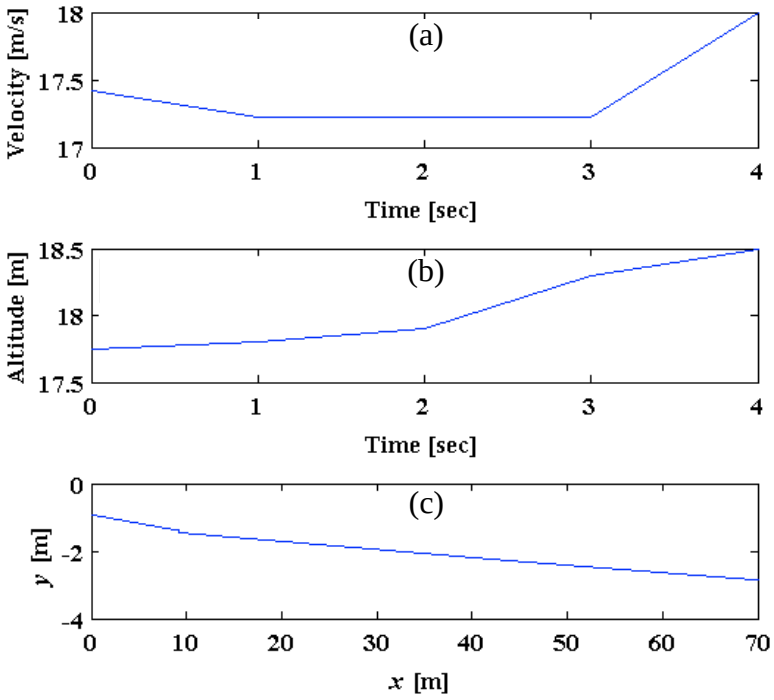

Figure 3.7. Simulated moving receiver with changing velocity, altitude, and trajectory: (a) velocity, (b) altitude, and (c) trajectory.

Similar to the acoustic excitation study, Fig. 3.8 – Fig. 3.10 show the normalized MUSIC power maps on the scanning area for each excitation type. Again, the maximum MUSIC power location estimation in each figure coincides with each source's location coordinates. Thus, it can be concluded that each source's location estimation is properly estimated.

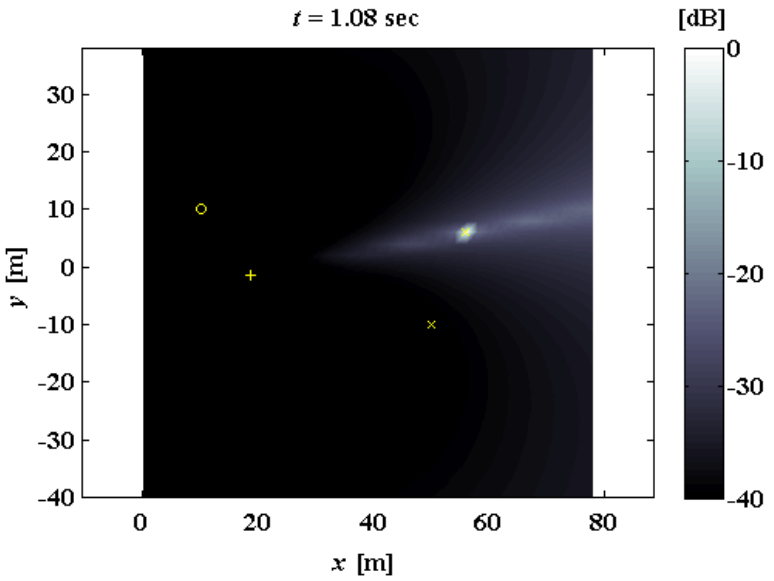

Figure 3.8. Normalized MUSIC power map at *t* = 1.08 sec estimating the sine source's location using simulated flight conditions.

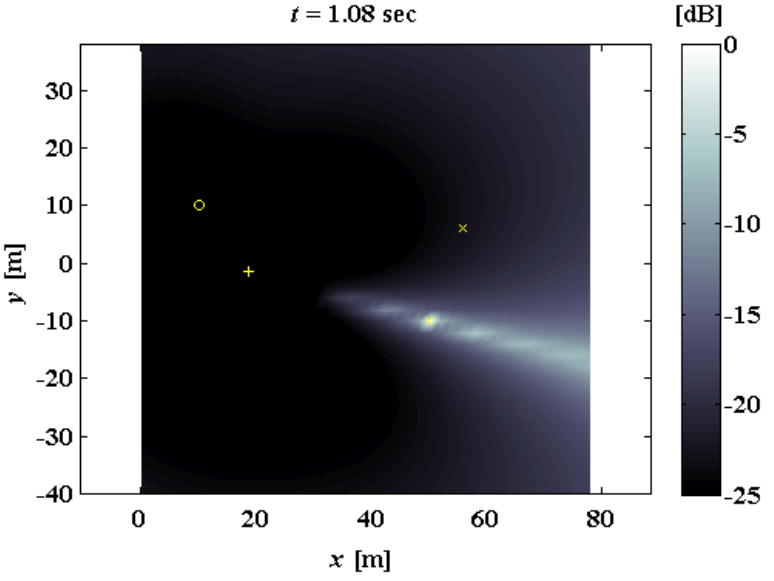

Figure 3.9. Normalized MUSIC power map at *t* = 1.08 sec estimating the banded white noise source's location using simulated flight conditions

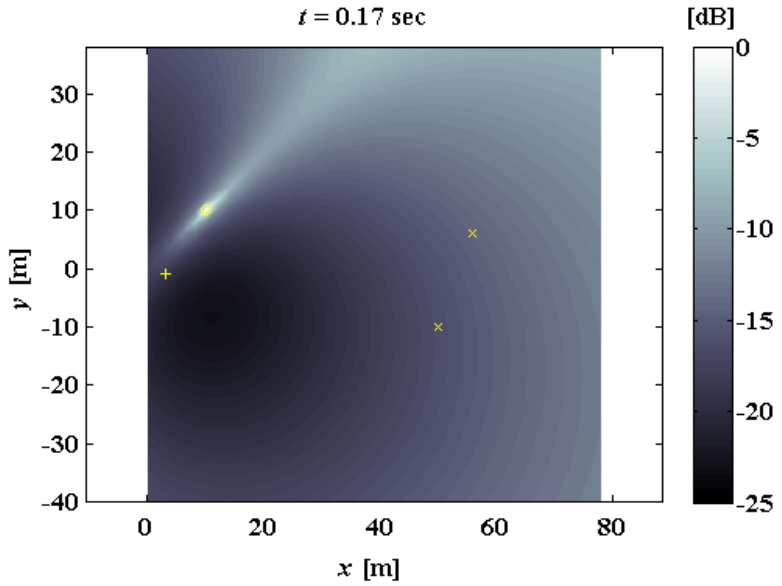

Figure 3.10. Normalized MUSIC power map at *t* = 0.17 sec estimating the impulse source's location using simulated flight conditions

3.3.3 Effects of multiple sources

In this study all three sources described in Table 3.1 are excited simultaneously using a constant velocity, altitude and trajectory as explained in Fig. 3.7.

Fig. 3.11 shows the normalized MUSIC power map of the scanning area with three different simultaneously excited sources. Fig.3.11 considers a constant simulated velocity, altitude and flight trajectory (see Fig.3.3). In Fig. 3.11 the largest normalized MUSIC power estimations coincide with each source's respective location coordinates; this is true for all time steps in the simulation.

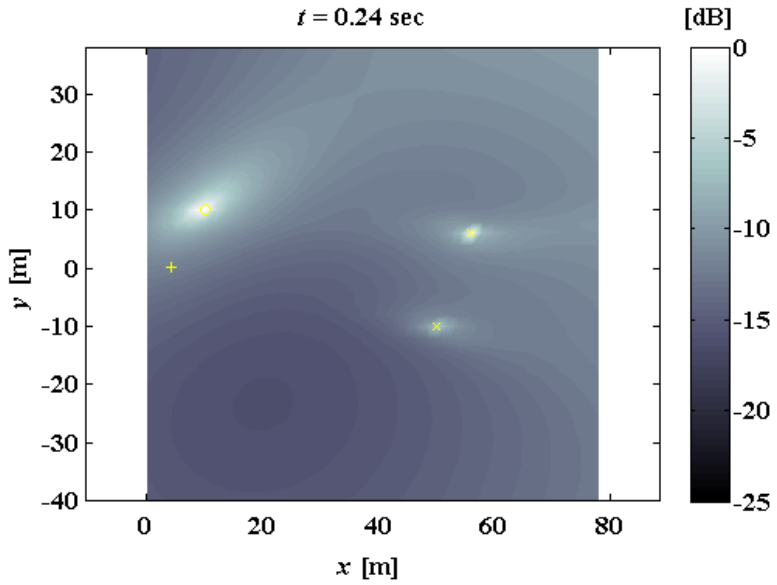

Figure 3.11. Normalized MUSIC power map detecting three simultaneously excited sources with constant flight conditions.

3.3.4 Distance error and angle error analysis

For this study only the sine and the banded white noise sources were considered with the constant simulated flight conditions described in Fig. 3.3. A distance error and absolute angle error analysis is explored to see how microphone location affects the algorithm's capability in estimating the simulated monopole's proper location coordinates. Distance error, d_{err}, is defined as the absolute distance between the simulated monopole's location coordinates and the coordinates where maximum MUSIC power is estimated. The monopole's angle, θ_s, is created between the simulated moving receiver's origin, the receiver's x-axis, and the simulated monopole's location coordinates. The estimated location angle, θ_e, is created between the simulated receiver's

origin, the receiver's x-axis, and the estimated coordinates with the maximum MUSIC power, as shown in Fig. 3.12.

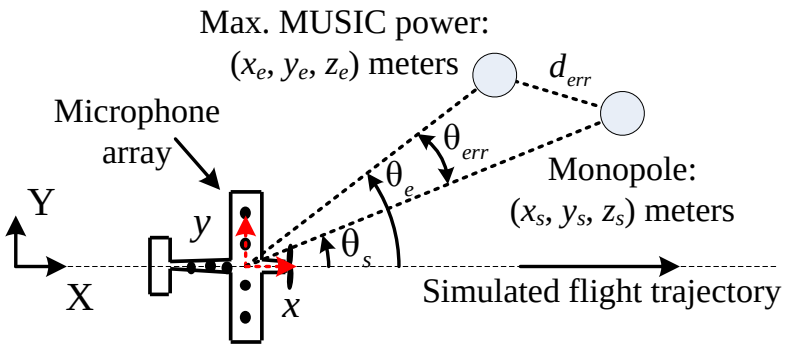

Figure 3.12. Definitions for distance error and angle error.

$$d_{err} = \sqrt{(x_s - x_e)^2 + (y_s - y_e)^2 + (z_s - z_e)^2} \tag{3.1}$$

$$|\theta_{err}| = |\theta_s - \theta_e| \tag{3.2}$$

Fig. 3.13 shows the corresponding distance and angle error for the 600 Hz sine monopole considering zero microphone error. From this figure, the zero distance and angle error is a result from having the MUSIC power map's estimated location coordinates always coinciding with the tonal source's simulated location. Also, a distance and angle error analysis is explored using a maximum microphone error of 1 cm; as seen in Fig. 3.14. To calculate microphone location error, a random number between ±1 is chosen for each microphone coordinate. This random number is then multiplied by the desired maximum microphone error, in this case 1 cm, and added to the actual microphone location. From Fig. 3.14 the average distance error from the

monopole's location coordinates is about 7.43 m and the averaged absolute angle error is about 1.02 degrees.

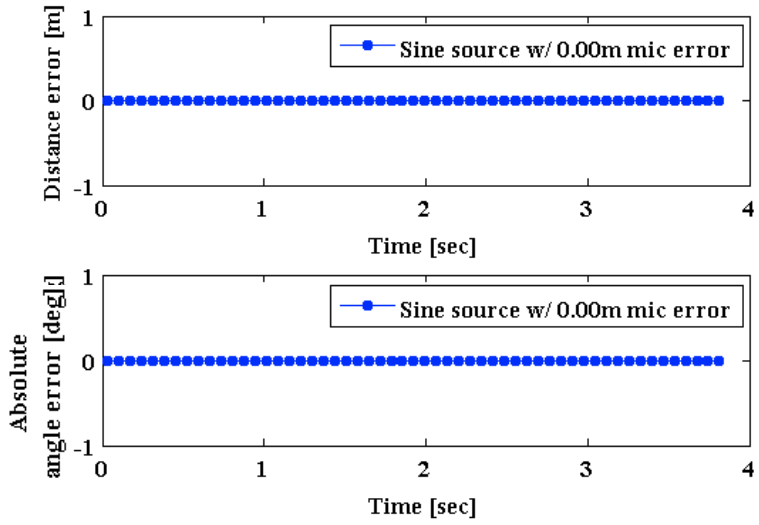

Figure 3.13. Distance error and angle error for the sine source considering zero microphone location error.

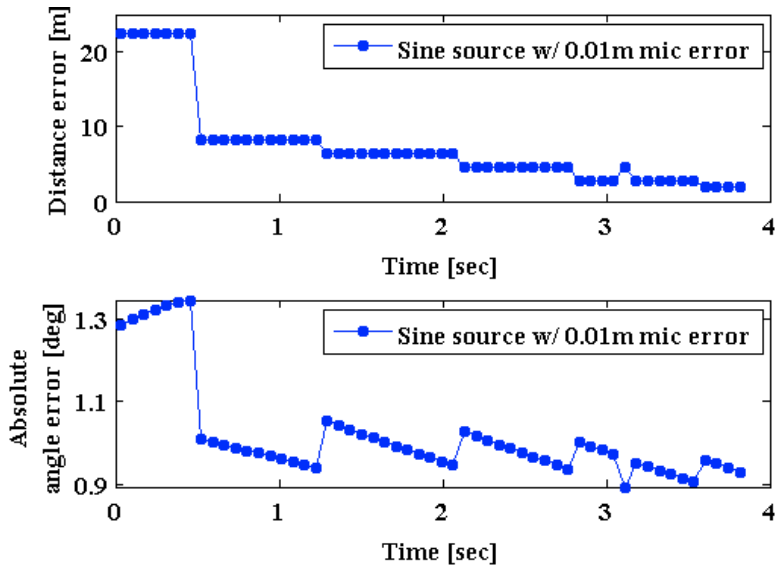

Figure 3.14. Distance error and angle error for the sine source considering a maximum microphone location error of 1 cm.

Additionally, Fig. 3.15 also shows the averaged distance error and averaged absolute angle error for the 600 Hz sine monopole for maximum microphone location error values 0 cm to 5 cm. This figure shows that small error in the microphone's location can lead to relatively large error when estimating the monopole's location in the far-field.

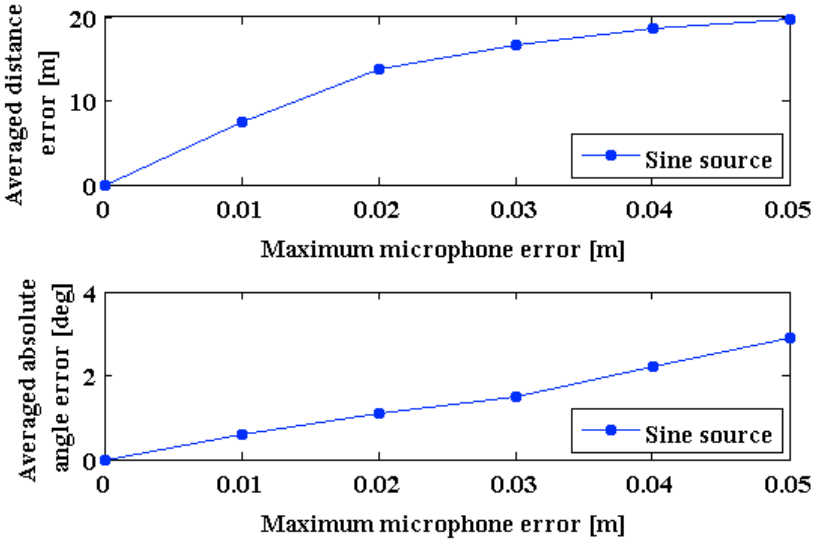

Figure 3.15. Averaged distance error and averaged absolute angle error for the sine source considering maximum microphone location error values 0 cm-5 cm.

Similarly, Fig. 3.16 shows the corresponding distance and angle error for the banded white noise monopole considering zero microphone error. Since the maximum MUSIC power is always estimated at the monopole's location coordinates, zero distance and angle error exist. Fig. 3.17 shows the error when considering a 1 cm maximum microphone location error. From this figure the average distance error from the

monopole's location is about 8.90 m and the averaged absolute angle error is about 0.58 degrees.

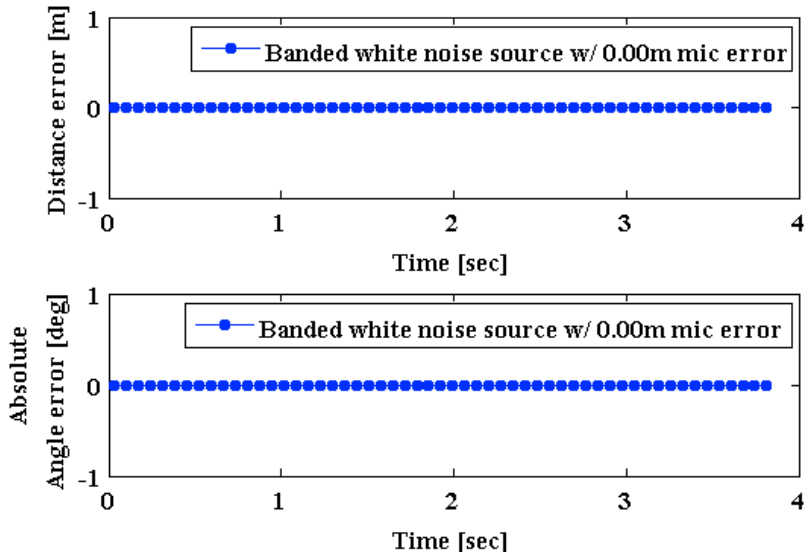

Figure 3.16 .Distance error and angle error for the banded white noise source considering zero microphone location error.

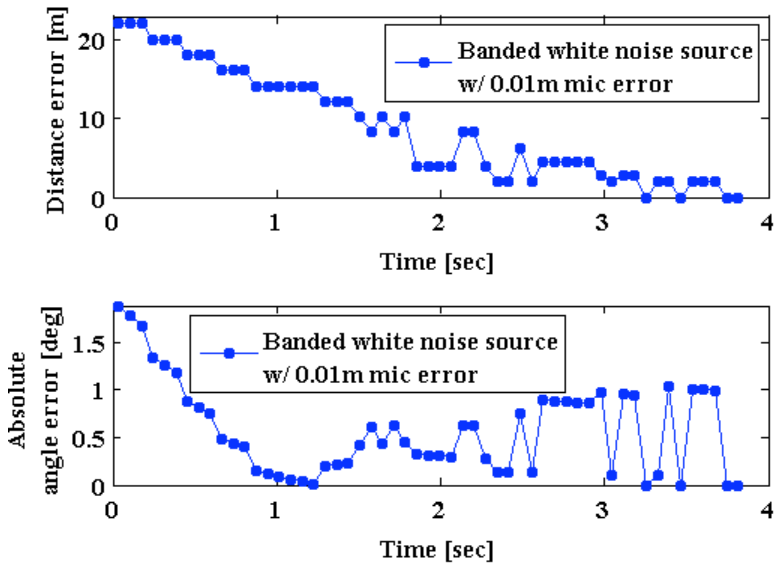

Figure 3.17. Distance error and angle error the banded white noise source considering a maximum microphone location error of 1 cm.

Additionally, Fig. 3.18 also shows the averaged distance error and averaged absolute angle error for the banded white noise monopole for maximum microphone location error values 0 cm to 5 cm. As expected, as the microphone location error is increased the distance and angle error also increases. It is worth noting that similar microphone location error behavior is seen when multiple sources are excited simultaneously.

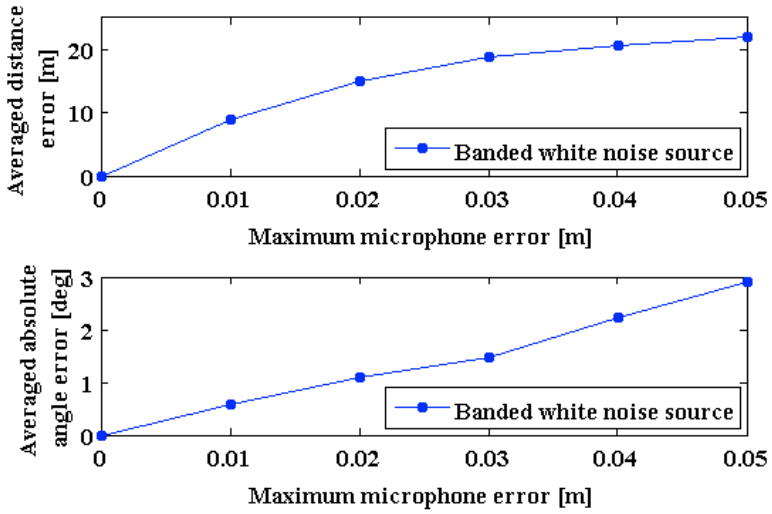

Figure 3.18. Averaged distance error and averaged absolute angle error for the banded white noise source considering maximum microphone location error values 0 cm-5 cm.

3.4 Simulated flight test summary

In this chapter the simulated flight test setup, processing procedure and results are presented. To test the proposed algorithm's performance three parameters were examined: (1) the acoustic excitation type; (2) the moving receiver's simulated flight conditions; and (3) the number of acoustic sources. Also, a distance error and angle error analysis is done to quantify the proposed algorithm's source location estimation accuracy when considering microphone location uncertainty.

The proposed algorithm accurately detected the monopole's location coordinates no matter the excitation type. This was also the case when considering constant or changing flight conditions, i.e. velocity, altitude and flight trajectory. When considering multiple simultaneously excited monopoles, at a relatively large altitude of 50 m, the algorithm was successful in locating all sources with zero error for all time *t*. Finally, a

distance and angle error analysis was conducted for the continuous sources, i.e. sine monopole and banded white noise monopole. The error analysis exposed how relatively small microphone location error, e.g. maximum 1cm location error, can propagate into large monopole averaged distance error of about 10 m in the far-field for all excitation types. Angle error is found to be less sensitive to microphone positioning uncertainty; for all simulations the averaged absolute angle error remained small, e.g. less than 4 degrees, even when considering a 5 cm maximum microphone location error.

4. LABORATORY TESTING

In this chapter the laboratory experiment setup, processing procedures, and results are presented. For experimental validation, three laboratory experiments were conducted. Source location estimations were done for: a 600 Hz sine source, a banded white noise source between 700-800 Hz and when both sine and banded white noise sources were excited simultaneously.

4.1 Laboratory experiment setup

In order to validate the proposed algorithm and data acquisition hardware, laboratory testing was conducted. In Fig. 4.1 a T-shaped array of 7 PIU Audio microphones (model: ROM-2238P-NF-R, see Table 4.1) is attached to the outer-bottom surface of the UAV and permanently fixed using epoxy. The location coordinates for the array microphones are seen in Table 4.2. An 8^{th} microphone is placed behind the electric engine to collect engine noise. A Hobby-Lobby Senior Telemaster Plus remote control (RC) plane is used as the UAV. This plane has a 96 inch wingspan and a 64 inch long fuselage.

One 14.8 V 4-cell 1350 mAh lithium-polymer (LiPo) battery powers the array microphones and the data collection hardware. Two 11.1V 4-cell 4400 mAh LiPo batteries are used to power all the UAV control surfaces, including the electric engine. Also, one transmitter-receiver set manages all the control surfaces, the engine speed and the data collection triggering.

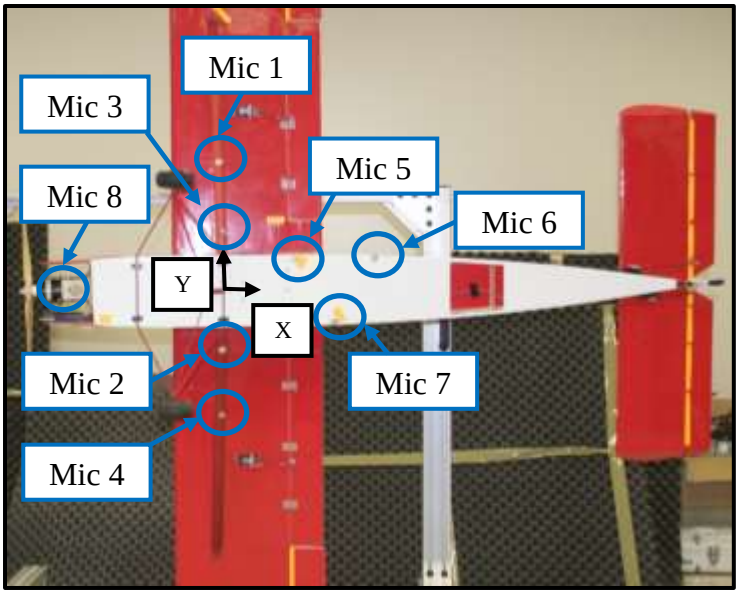

Figure 4.1. Microphone array configuration for laboratory tests.

Table 4.1. PUI Audio (ROM-2238P-NF-R) microphone specifications.

Parameter	Value	Unit
Directivity	Omni	-
Sensitivity	-38 ± 3	dB
Max. Operating Voltage	10	Vdc
Stnd. Operating Voltage	2.0	Vdc
Max. Current Consumption	0.5	mA
Impedance	2.2	kΩ
Signal to Noise Ratio	60	dB
Terminal	PIN	-
Diameter	5.8 ± 0.1	mm
Depth	2.2 ± 0.2	mm

Table 4.2. Array microphone locations for laboratory testing.

Microphone	x_m [m]	y_m [m]	z_m [m]
1	0	0.295	-0.072
2	0	-0.132	-0.020
3	0	0.132	-0.020
4	0	-0.295	-0.072
5	0.155	0.072	-0.006
6	0.345	0.067	-0.007
7	0.245	-0.075	-0.006

For laboratory testing the UAV was positioned with its wings held at vertical as seen in Fig. 4.2 by an aluminum frame. Each experiment's excitation type, number of sources, location coordinates, SPL, and duration can be seen in Table 4.3. Also, the Brüel & Kjær (B&K) Labshop software and two M-Audio speakers (mode: BX5a-Deluxe) were used to generate the tonal and banded white noise signals.

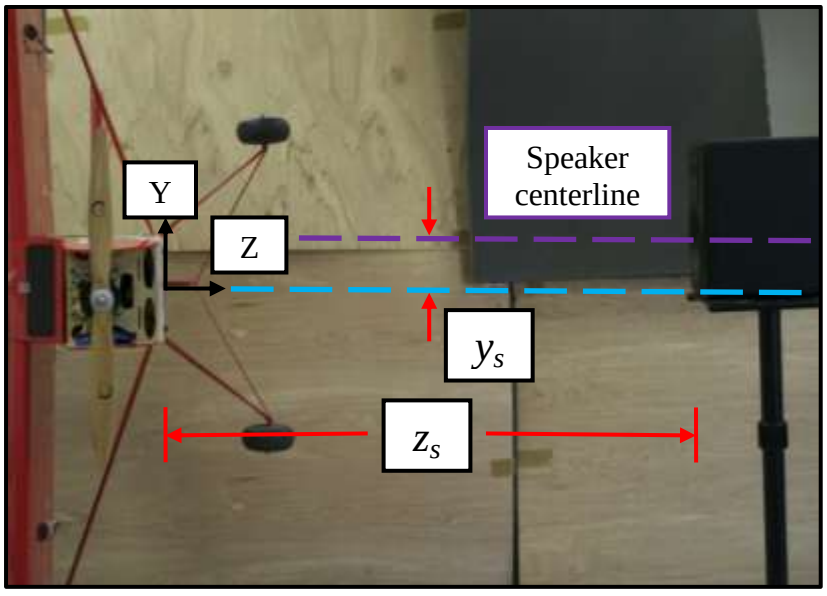

Figure 4.2. The speaker's relative location with respect to the UAV's coordinate origin.

Table 4.3. Laboratory test parameters.

Excitation	No. of sources	Location (x_s, y_s, z_s) [m]	SPL [dB/20μPa]	Duration [sec]
Sine (600 Hz)	1	(-0.6, 0.1, 4.6)	100	4
White noise (700-800 Hz)	1	(1.2, -0.3, 4.6)	80	4
Sine (600 Hz); White noise (700-800 Hz)	2	(-0.6, 0.1, 4.6)	100	4
		(1.2, -0.3, 4.6)	80	4

For data collection, the National Instruments (NI) compactRIO (cRIO) data acquisition (DAQ) was secured inside the fuselage then connected to the microphones and corresponding LiPo battery. The entire cRIO DAQ is packaged in a 3.5 inch × 3.5 inch × 7.0 inch volume. As seen in Fig. 4.3, the cRIO DAQ is comprised of 5 components: one 4-slot reconfigurable chassis (NI cRIO-9113), one real-time 256 MB DRAM controller (NI cRIO-9022), two 4-channel ± 5V & 51.2 kS/s per channel analog module (NI 9234), and one 4-channel 50ns LVTTL digital module (NI 9402). In-house code was developed for the cRIO DAQ using LabVIEW along with the NI Field-Programmable Gate Array (FPGA) and NI Real-Time (RT) software modules. The LabVIEW code initiates and ceases data collection by monitoring the digital signal from one specific channel on the receiver, this channel is controlled by its corresponding transmitter toggle switch. Appendix A contains further explanations for the LabVIEW code.

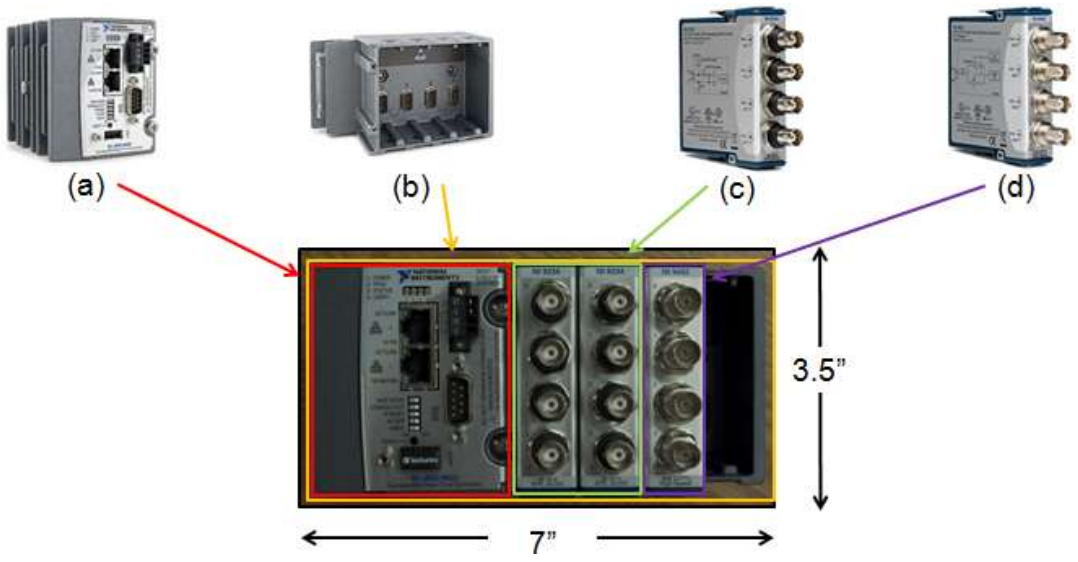

Figure 4.3. NI cRIO DAQ for data collection: (a) RT controller, (b) 4-slot chassis, (c) 4-channel analog module and (d) 4-channel digital module.

4.2 Laboratory experiment processing procedure

For the laboratory test experiments, the same algorithm used for the simulation validation is used here in the laboratory testing; except the UAV's velocity is considered to be zero. Similar to the numerical simulations, 4 seconds of sound pressure data sampled at f_s = 3.657 kHz is collected from the M-Audio speakers. To process this data: the initial time step, $t_{1,}$ is 512 / f_s = 0.140 seconds; the extracted data length, N, is 1024 data points; the Hanning window length, D, is 256 data points; and the zero vector length, L, is 1024 data points. A larger extracted data length, N, and Hanning window length, D, was chosen to process the laboratory results in attempt to include more averaged CSMs to mitigate truncation noise in the laboratory.

Let $\mathbf{x}(t_1)$ define a time block of 7 × 1024 data points extracted from the total sound pressure field data centered at t_1 = 0.140 seconds. While maintaining its indexed locations, a windowed 7 × 256 section of $\mathbf{x}(t_1)$, starting at τ_1 = 0 seconds, is extracted and placed into a 7 × 1024 zero matrix. Then, an instantaneous 7 × 7 CSM is calculated for each frequency. The 7 × 256 Hanning window is then moved to start at τ_2 = 0.420 seconds and reapplied to $\mathbf{x}(t_1)$. This second set of windowed data is also placed into another 7 × 1024 zero matrix and an instantaneous 7 × 7 CSM is calculated for each frequency. Each CSM is added the previous until all the point within $\mathbf{x}(t_1)$ have been windowed. Then, the $\mathbf{R}_{avg,1}(t_1,f)$ is calculated and SVD is applied. Finally, the time-frequency MUSIC power is calculated at each scanning point. The scanning area is a 41 × 41 grid spanning (X,Y) = ([-2,2],[-2,2]) m with $\Delta X = \Delta Y = 0.1$ m. This process repeats at the next time step until all 4 seconds of sound pressure data is processed.

4.3 Laboratory experiment results

Fig. 4.4 shows the normalized MUSIC power map of the scanning area at the 3.78 sec time step for the tonal source. Also, Fig. 4.5 shows the corresponding distance and angle error. In Fig.4.5 the average distance error from the speaker's location coordinates is about 0.90 m and the averaged absolute angle error is about 14.07 degrees.

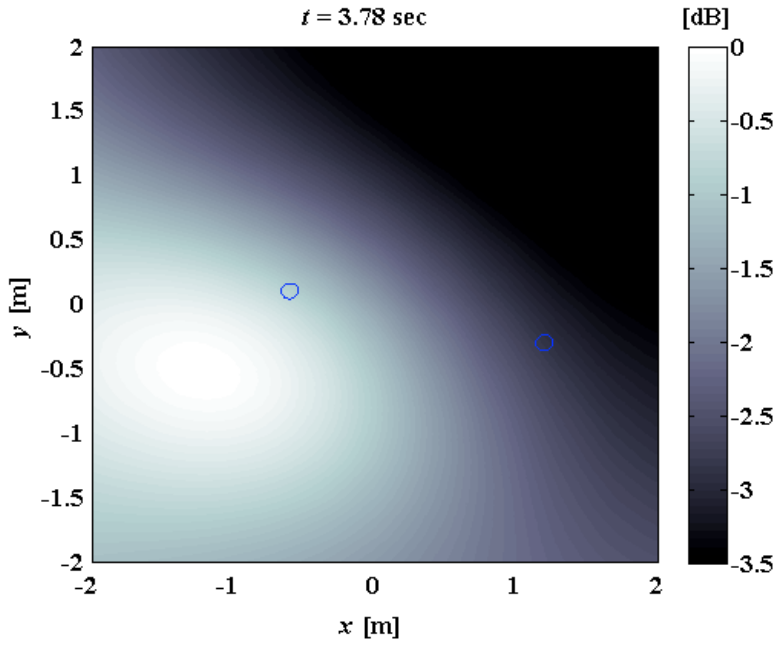

Figure 4.4. Normalized MUSIC power map at t = 3.78 sec estimating the tonal source's location in laboratory testing.

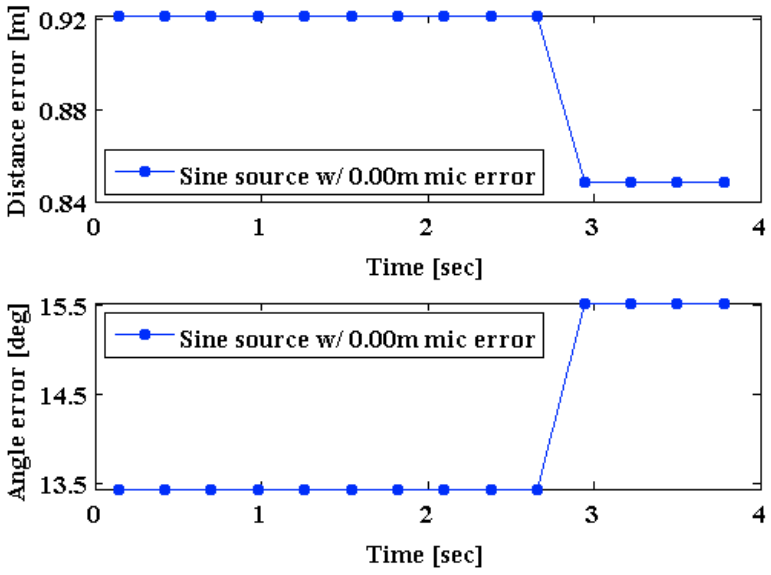

Figure 4.5. Distance error and angle error for the tonal source in laboratory testing.

Similarly, Fig. 4.6 shows the normalized MUSIC power map of the scanning area at the 2.10 sec time step for the banded white noise source. Fig. 4.7 shows the corresponding distance and angle error. In Fig.4.7 the average distance error from the speaker's location coordinates is about 1.09 m and the averaged absolute angle error is about 47.14 degrees.

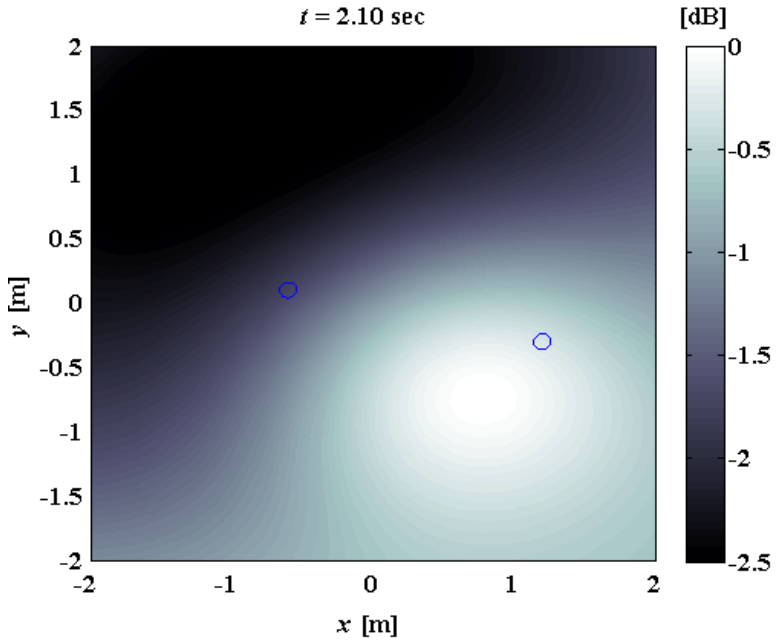

Figure 4.6. Normalized MUSIC power map at *t* = 2.10 sec estimating the banded white noise source's location in laboratory testing.

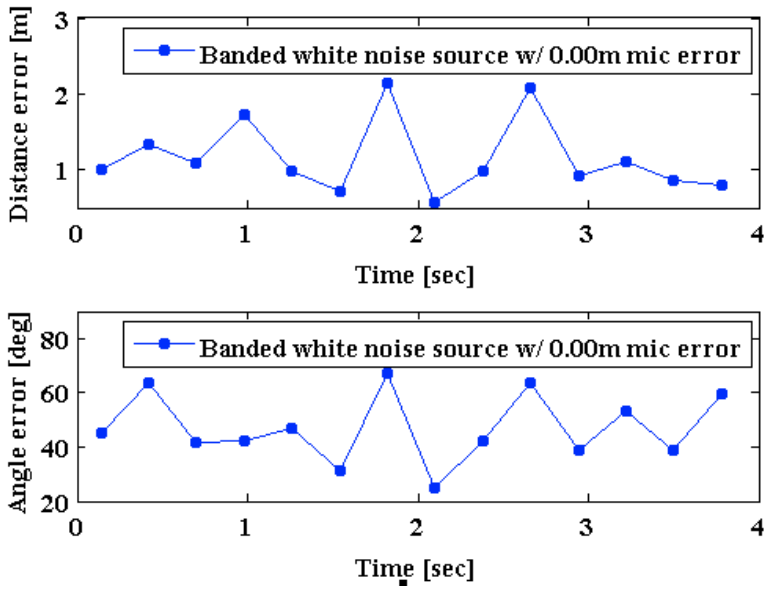

Figure 4.7. Distance error and angle error for the banded white noise source in laboratory testing.

Finally, Fig. 4.8 shows the normalized MUSIC power map of the scanning area at the 1.26 sec time step for the simultaneous excitation of the tonal source and the banded white noise source. Fig. 4.9 shows the corresponding distance and angle error. In Fig.4.9 the average distance error from the speaker's location coordinates is about 0.78 m and the averaged absolute angle error is about 8.14 degrees.

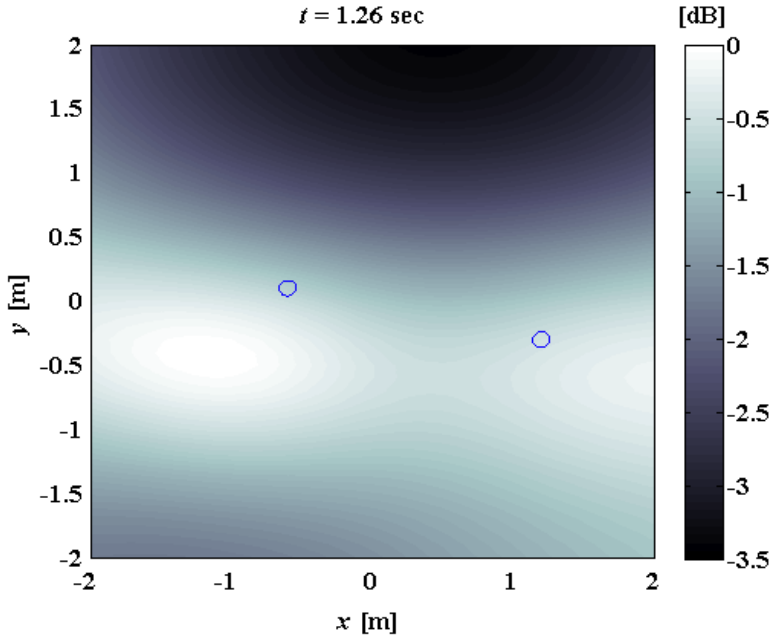

Figure 4.8. Normalized MUSIC power map at *t* = 1.26 sec for detecting two simultaneously excited sources in laboratory testing.

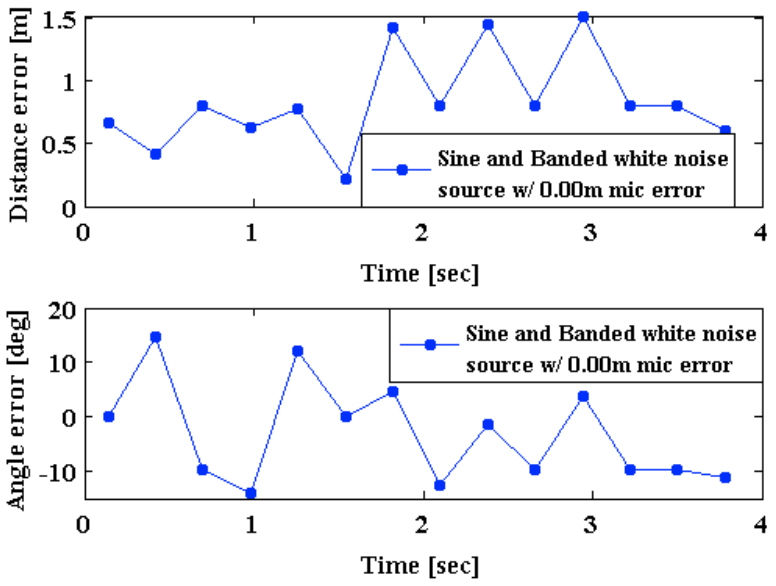

Figure 4.9. Distance error and angle error for detecting two simultaneously excited sources in laboratory testing.

Since the laboratory experiments are in such a controlled environment it was hard to believe that microphone location error was solely responsible for estimated location error of this magnitude. After initial troubleshooting, the source estimated location error is believed to come from a hardware issue and not a problem with the time-frequency MUSIC beamforming algorithm or its processing. It is believed that the hardware might be calibrated incorrectly or have some internal damage that does not allow the sound pressure data collected by the PIU Audio microphones to be measured correctly.

An identical laboratory setup, as the one proposed in section 4.1, is currently being built to validate the author's hardware diagnosis. For the troubleshooting setup, sound pressure data will be collected using 7 one-quarter inch B&K microphones (Type: 4958) placed in the same array configuration described in Table 4.2. Also, two B&K PULSE portable DAQ systems (model: 3560-B-130) are used to collect the sound pressure data from all 7 B&K microphones using the B&K Labshop software.

4.4 Laboratory experiment summary

In this chapter the laboratory experiment setup was presented. This included information about: the Sr. Telemaster Plus RC plane to serve as the UAV; the microphone array configuration; the microphones in the array; and, finally, the proposed NI cRIO DAQ. Also, the laboratory experiment processing procedure and results were shared.

Three laboratory experiments were conducted. Source location estimations were done for: a 600 Hz sine source, a banded white noise source between 700-800 Hz and when both sine and banded white noise sources were excited simultaneously. The sine source had an average distance error and averaged absolute angle error of 0.9 m and 14.07 degrees from the source's true location, respectively. Similarly, the banded white noise source's average distance and absolute angle error was 1.9 m and 47.14 degrees; and lastly, an average distance and absolute angle error of 0.78 m and 8.14 degrees resulted after exciting both sources simultaneously. It is believed that most of the estimated location error is caused by the cRIO DAQ not correctly measuring the sound pressure data collected by the array microphones. Current research is underway, using a second troubleshooting experimental setup, to verify whether the cRIO DAQ is functioning correctly.

5. CONCLUSION AND RECOMMENDATIONS

5.1 Summary

When a microphone array is mounted on a mobile aerial platform, such as a UAV, most existing beamforming methods cannot be used to adequately identify continuous and impulsive ground sources. In this work, an improved time-frequency beamforming method based on the Multiple Signal Classification (MUSIC) algorithm is proposed to identify and locate these acoustic events. The objective of the preceding work in this thesis sought to validate the proposed algorithm with: (i) numerical simulations and (ii) laboratory experiments.

In this Chapter 1 a concise introduction is given into: early acoustic arrays and UAVs in the battlefield, array signal processing techniques, and current sound source localization literature using aerial acoustic sensor arrays. In Chapter 2 the sound pressure field equation for a stationary monopole, a stationary medium and a moving receiver is derived. Also, the proposed time-frequency MUSIC beamforming algorithm is explained. In Chapter 3 the simulated flight test setup, processing procedure and results are presented. Likewise, in Chapter 4 the laboratory experimental setup, processing procedure, and results are also presented.

5.2 Conclusions

In the numerical simulations three parameters were varied to test the proposed algorithm's location estimation performance: 1) the acoustic excitation type; 2) the moving receiver's simulated flight conditions; and 3) the number of acoustic sources.

Also, a distance and angle error analysis was done to quantify the proposed algorithm's source location estimation accuracy when considering microphone positioning uncertainty.

The proposed algorithm accurately detects the simulated monopole's location coordinates with zero error no matter the excitation type, i.e. tonal, banded white noise, or impulse, or simulated flight conditions. When considering multiple simultaneously excited monopoles at an altitude of 50 m the proposed algorithm had no error when estimating the source's locations. Finally, a distance and angle error analysis was conducted for the continuous sources, i.e. the tonal monopole and the banded white noise monopole. The error analysis exposed how relatively small microphone location error, e.g. 1 cm maximum error, can propagate into large monopole distance error of about 10 m in the far-field. In summary, the numerical simulations verified the proposed time-frequency MUSIC beamforming algorithm's capability in estimating acoustic target locations in addition to DOA.

For experimental validation, three laboratory experiments were conducted. Source location estimations were done for: a 600 Hz sine source, a banded white noise source between 700-800 Hz and when both sine and banded white noise sources were excited simultaneously. The algorithm was able to constantly estimate the speaker's location coordinates; however, some distance and angle error is present. The sine source had an average distance error and averaged absolute angle error of 0.9 m and 14.07 degrees from the source's true location, respectively. Similarly, the banded white noise source's average distance and absolute angle error was 1.9 m and 47.14 degrees; and

lastly, an average distance and absolute angle error of 0.78 m and 8.14 degrees resulted after exciting both sources simultaneously. Initial troubleshooting experiments indicate most of the estimated location error is caused by the microphone's lack of sensitivity and not the cRIO DAQ. More research is underway, using a second troubleshooting experimental setup, to verify whether the source location estimations can be improved using cRIO DAQ and proposed algorithm. Although it appears that sound pressure data is not accurately measured by the cRIO DAQ, the laboratory experiments verify that the proposed time-frequency MUSIC beamforming algorithm is still capable in estimating single and multiple monopole sources. Once this hardware issue is remedied, it is believed that estimation error will dramatically decrease to within a few centimeters.

5.3 Future work & recommendations

Figure 5.1. The Senior Telemaster Plus RC plane used for flight testing.

For flight testing, the same Sr. Telemaster Plus (see Fig. 5.1), microphone array geometry, data acquisition and wiring are used as described in section 4.1; however,

unlike the laboratory experiments, two transmitter and receiver sets are used for flight testing. One transmitter and receiver set manages all the control surfaces and the engine speed on the UAV while the second transmitter and receiver set serves for data triggering and collection. Also, GiSTEQ^{TM} GPS data logger is secured onboard the UAV to track its latitudinal coordinates, longitudinal coordinates and velocity.

For experimental flight testing, an open airfield divided into three flight conditions is proposed. During each test the UAV will go through: a gliding condition, an engine ON condition, and an engine ON with acoustic sources condition. When the plane is in the gliding section, the engine is OFF and the plane glides at a specified altitude. This flight condition serves to identify the noise due to air flow. Upon entering the second section, the electric engine is turned ON. This flight condition serves to identify noise contributed from the electric engine. Finally, when entering the final section, the engine remains ON and the acoustic sources are also turned ON. Fig. 5.2 shows the three flight conditions with the acoustic source locations.

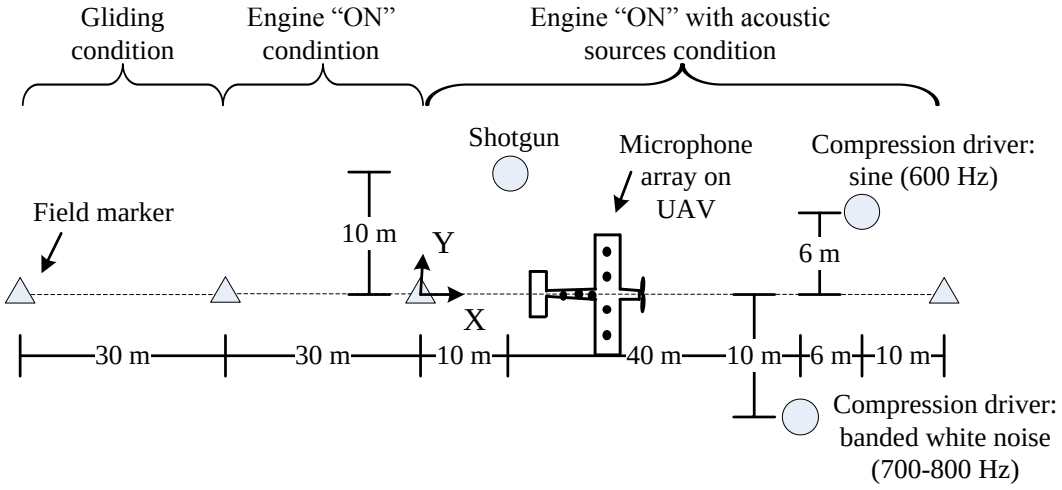

Figure 5.2. Proposed flight experiment field layout.

A 12 gauge shotgun, shooting blank shells, serves as the impulse acoustic source while two JBL-2446H compression drivers are used, in conjunction with the B&K portable PULSE DAQ and software, to generate a 600 Hz sine wave and a banded white noise signal between 700 Hz and 800 Hz. The proposed time-frequency MUSIC beamforming algorithm proposed in this work can be used to process the flight data information.

Before conducting flight experiments, three recommendations are strongly suggested. 1) Replace current array microphones with more sensitive microphones with better SNR. 2) Change microphone array configuration where most microphones would be along the same plane. Lastly, 3) sync data collection and GPS data logger to allow easier post-processing.

REFERENCES

[1]B. Kaushik, D. Nance, and K. K. Ahuja, “A Review of the Role of Acousic Sensors in the Modern Battlefield.” AIAA/CEAS Aeroacoustics Conference (2005)

[2]T. Ehrhard, "Air Force UAVs: A Secret History." Air Force Association. Mitchell Institute Press, Jul 2010. Web. (2012). http://www.afa.org/mitchell/reports/MS_UAV_0710.pdf

[3]K. C. Wong, C. Bil, D. Gordon, and P. W. Gibbens, "Study of the Unmanned Aerial Vehicle (UAV) Market in Australia", Aerospace Technology Forum Report (1997).

[4]C. Y. Chong, S. P. Kumar, and B. A. Hamilton, “Sensor Networks: Evolution, Opportunities, and Challenges,” Proc. IEEE, 91, 1247-1256 (2003).

[5]H. Krim and M. Viberg, "Two Decades of Array Signal Processing Research: The Parametric Approach," Signal Processing Magazine IEEE , 13, 67-94 (1996).

[6]B. D. Van Veen and K. M. Buckley. “Beamforming: A Versatile Approach to Spatial Filtering,” IEEE ASSP Magazine, 4-24 (1988).

[7]G. Bienvenu and L. Kopp. “Adaptivity to Background Noise Spatial Coherence for High Resolution Passive Methods.” lnt. Conf. on Acoust., Speech and Signal Processing, 307-310 (1980).

[8]R. O. Schmidt. “A Signal Subspace Approach to Multiple Emitter Location and Spectral Estimation.” Ph.D. thesis, Stanford Univ., Stanford, CA. (1981).

[9]B. M. Sadler, T. Pham, L. C. Sadler, "Optimal and Wavelet-Based Shockwave Detection and Estimation," Journal of the Acoustic Society of America, Vol. 104, No. 2, Pt. 1, pp. 955-963, 1998.

[10]B. Ferguson, "Locating Far-Field Impulsive Sound Sources in Air by Triangulation," Journal of the Acoustic Society of America., Vol. 111, pp.104-116, 2002.

[11]R. J. Kozick, B. M. Sadler, "Source Localization with Distributed Sensor Arrays and Partial Spatial Coherence," IEEE Transactions on Signal Processing, Vol. 52, No. 3, pp. 601-616, 2004.

[12]T. Pham, N. Srour, "TTCP AG-6 Acoustic Detection & Tracking of UAV's," Proc. of SPIE, Unattended/Unmanned Ground, Ocean, and Air Sensor Technologies & Applications VI, Vol. 5417, April 2004.

[13]C. Reiff, T. Pham, M. Scanlon, J. Noble "Acoustic Detection from Aerial Balloon Platform," Proc. of the 24th Army Science Conference, Paper No. EP-11, Orlando FL, Nov 2004.

[14]M. Scanlon, C. Reiff, J. Noble, "Acoustic Transient Source Localization from an Aerostat," Proc. of the 25th Army Science Conference, Paper No. AP-24, Orlando FL, Oct 2006.

[15]C. Reiff, M. Scanlon, J. Noble, "Acoustic Detection and Localization from a Tethered Aerostat", Proceedings of SPIE, Volume 6231, May 2006.

[16]D. Robertson, T. Pham, H. Edge, B. Porter, J. Shumaker, D. Cline, "Acoustic Sensing from Small-Size UAVs," Proc. of SPIE, Volume 6562, 2007.

[17]B. Ferguson, R. Wyber, "Detection and Localisation of a Ground Based Impulse Sound Source Using Acoustic Sensor Onboard a Tactical Unmanned Aerial Vehicle," Proc. of NATO SET-107-RSY-20-MSE Symposium on Battlefield Acoustic Sensing for ISR Applications, Amsterdam, The Netherlands, October 2006.

[18] A. Hirschberg and S.W. Rienstra, *An Introduction to Aeroacoustics*, Cambridge University Press, Eindhoven, The Netherlands, pp.25-27, 2007.

[19] P.M. Morse and K.U. Ingard, *Theoretical Acoustics (Volume 2)*, Princeton University Press, Princeton, New Jersey, pp. 698-780, 1968.

[20] J.H. Han and Y.J. Kim. "Time-Frequency for Nondestructive Evaluations of Plate Using Ultrasonic Lamb Wave*."* Submitted to Journal of Sound and Vibration, 2011.

APPENDIX A

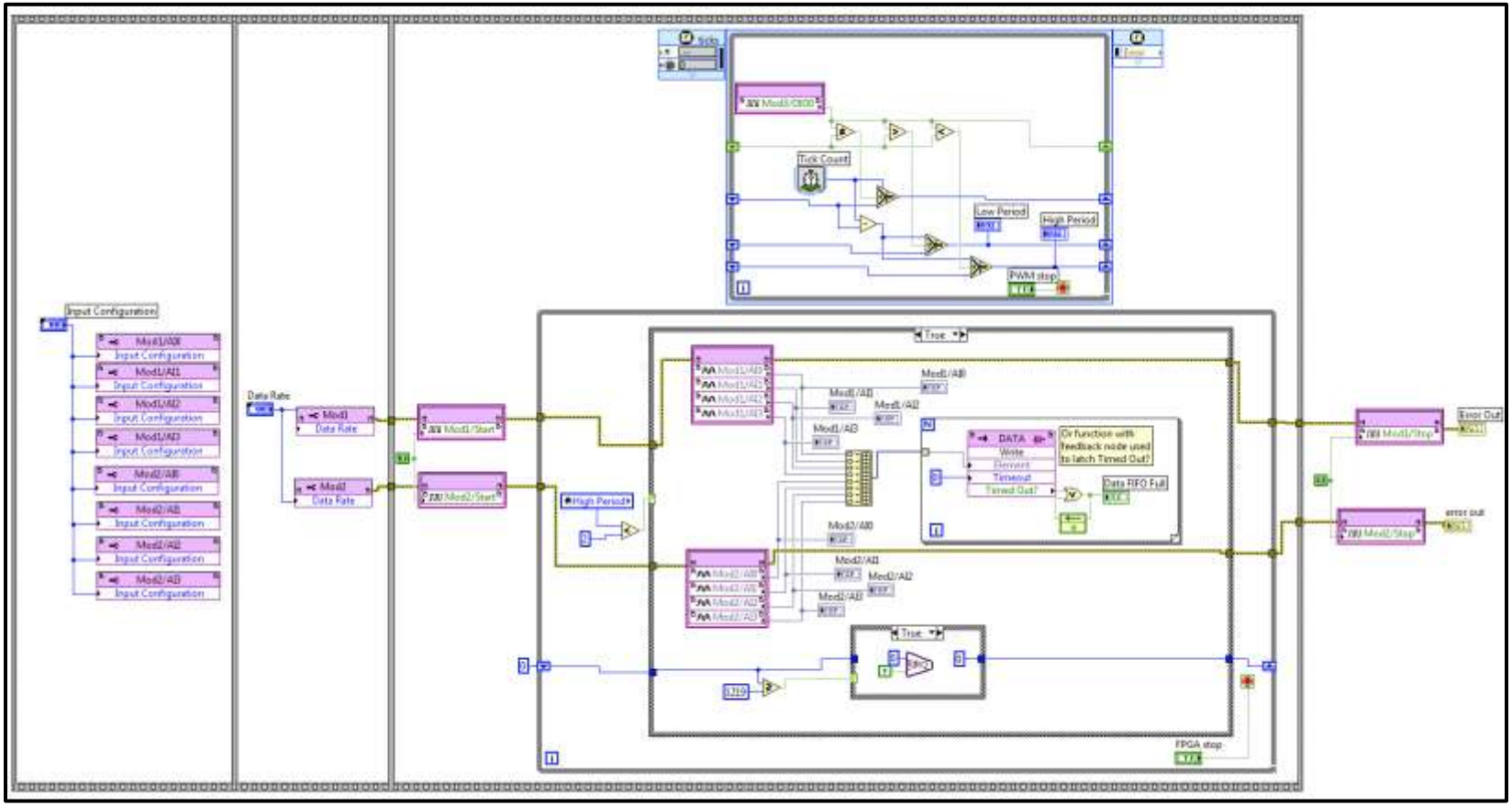

Figure A.1. cRIO FPGA code

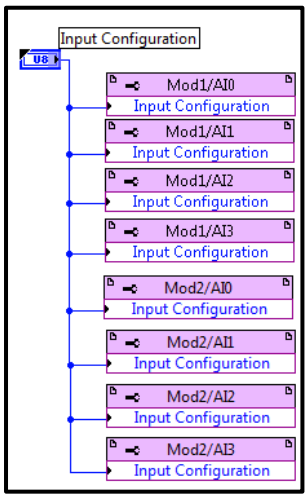

Figure A.2. Set desired input for all channels in module 1 & 2.

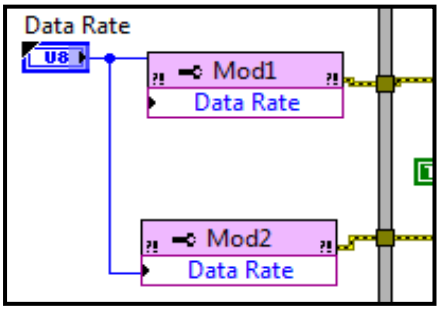

Figure A.3. Set desired data rate for all channels in module 1 & 2.

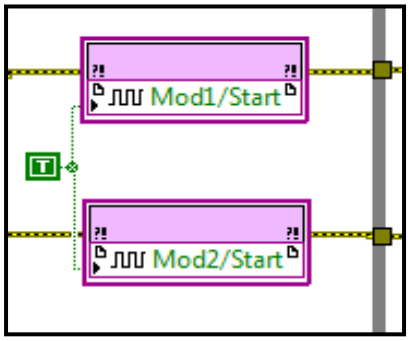

Figure A.4. Enable module 1 & 2 to start data collection.

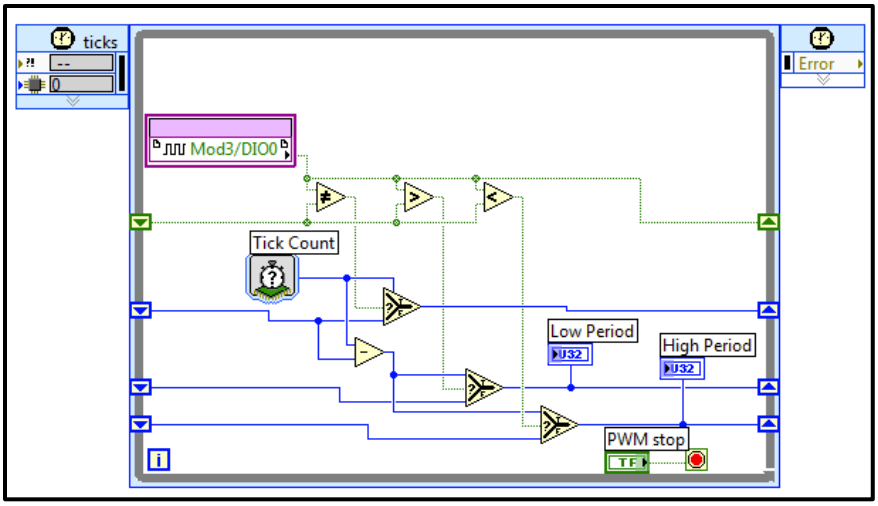

Figure A.5. Timed loop continuously measuring high & low period for the square wave measured from channel 0 in the digital I/O module.

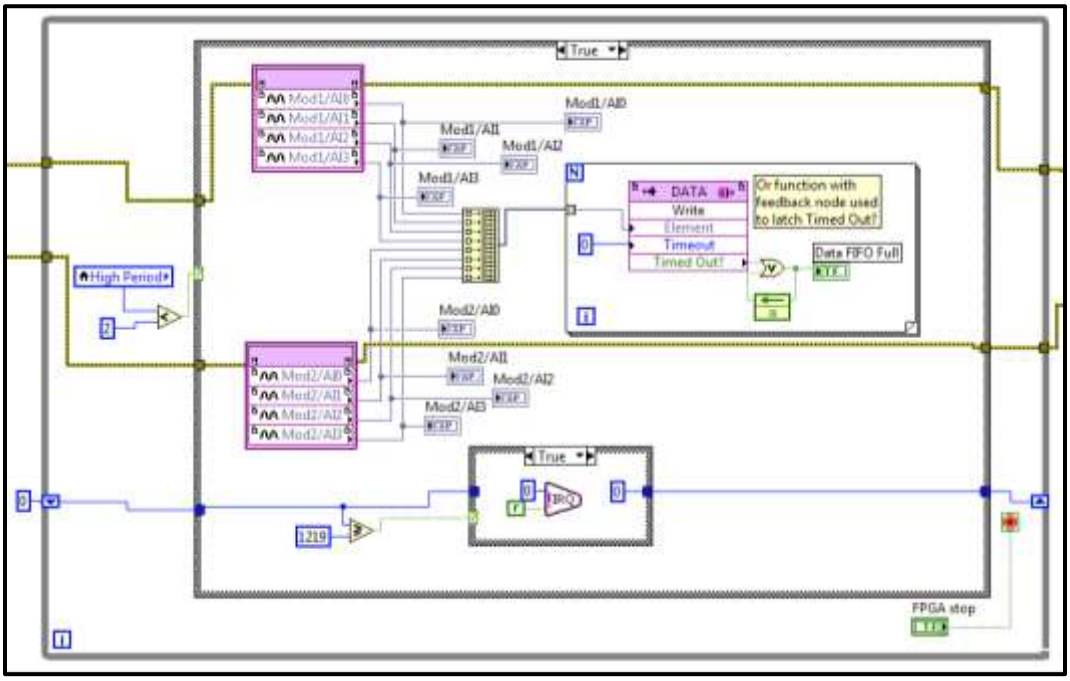

Figure A.6. Case structure nested in while loop that collects data when high period is less than 2 msec.

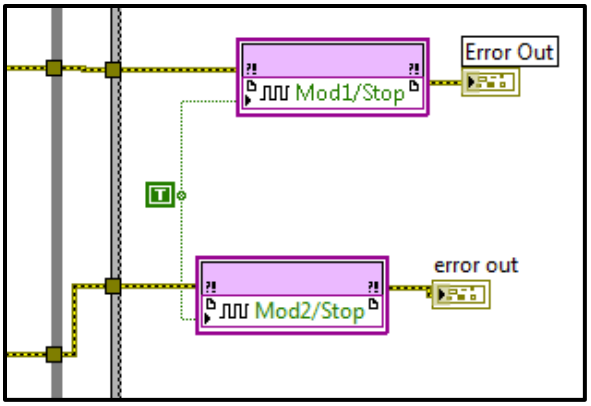

Figure A.7. Stop module 1 & 2 from collecting data.

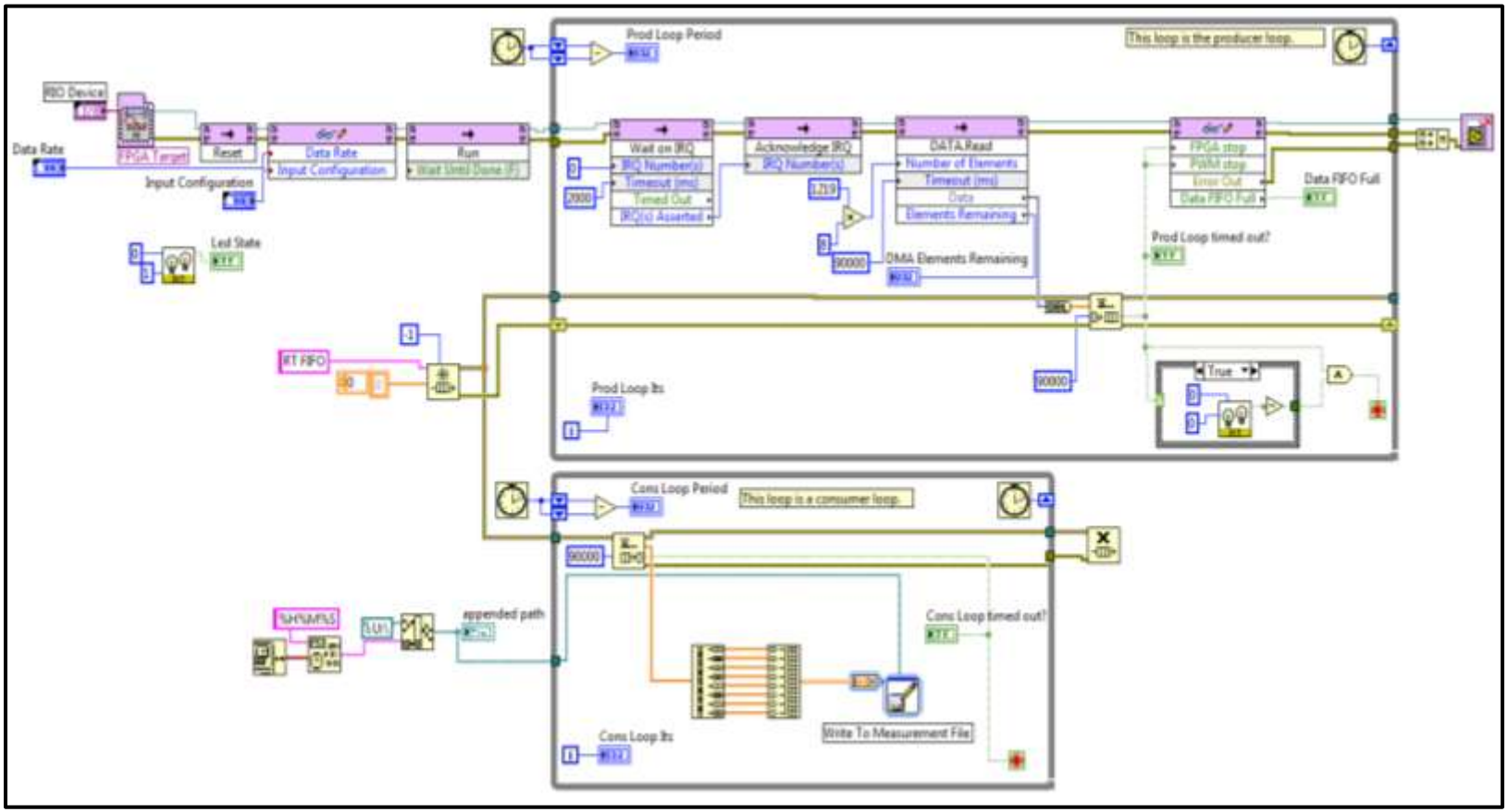

Fig. A.8. cRIO RT code

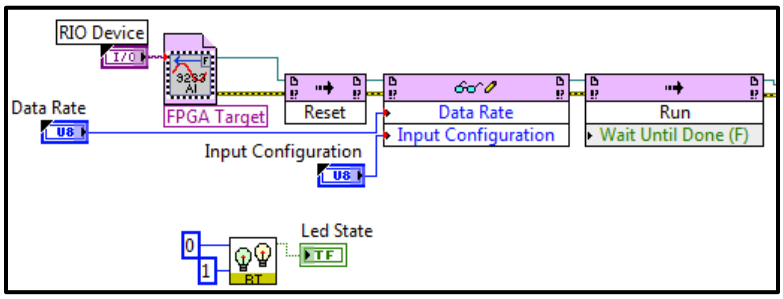

Figure A.9. Open FPGA reference target; write data rate and input configuration to FPGA target then run code; also, turn on LED indicator.

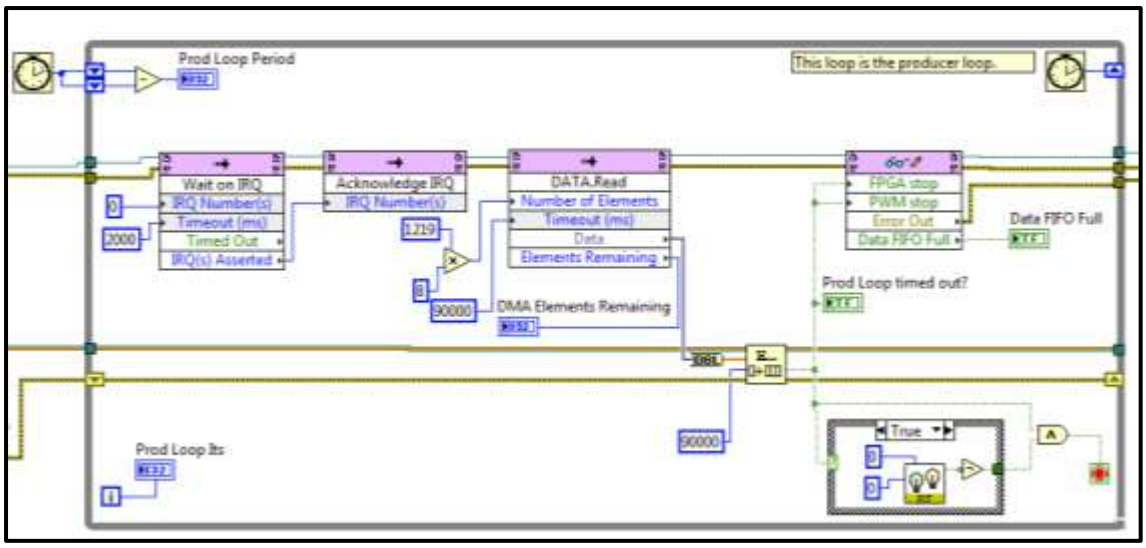

Figure A.10. Read data from FIFO; send data through enqueue to consumer loop; turn off FPGA and LED indicator when enqueue times out.

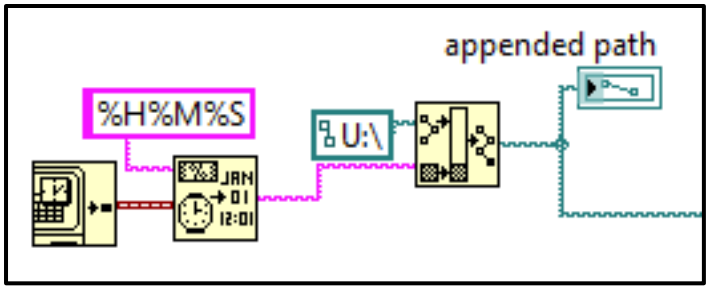

Figure A.11. Get time in hours, minutes, and seconds; build path to save on external USB; append path to "write to measurement" file.

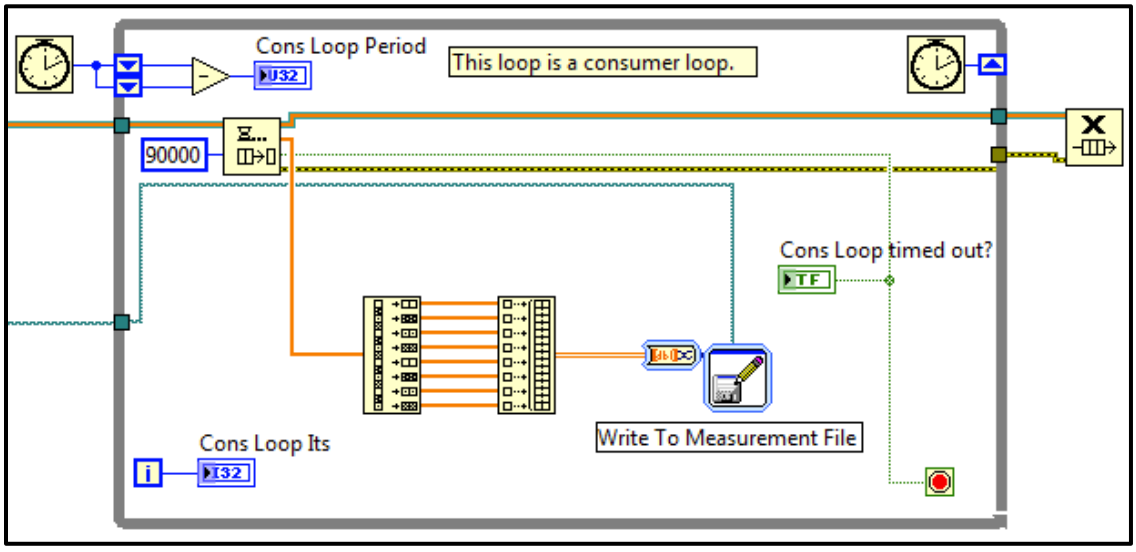

Figure A.12. Read data from enqueue block, restructure data to array format; save data to "write to measurement" file.

A.2. Loading code to compactRIO DAQ

Step 1: Connect computer to port 1 LAN connection on cRIO controller.

Step 2: Connect cRIO controller to power source using screw terminals and turn ON.

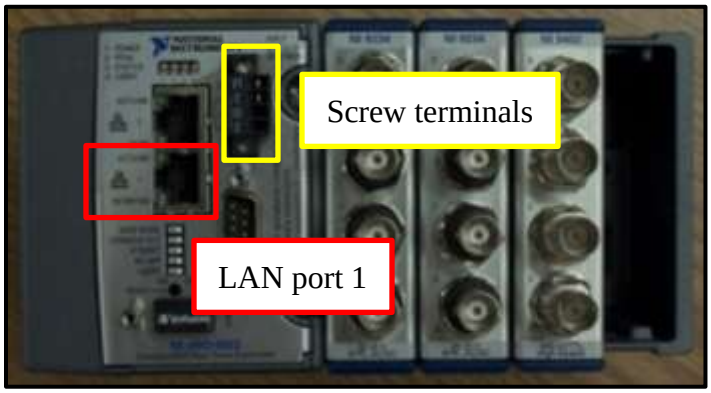

Figure A.13. LAN port 1 and screw terminal locations.

Step 3: Open current version of NI LabVIEW

Figure A.14. LabVIEW "Getting Started" home screen.

Step 4: Open desired project file. Project Explorer window will appear after opening project.

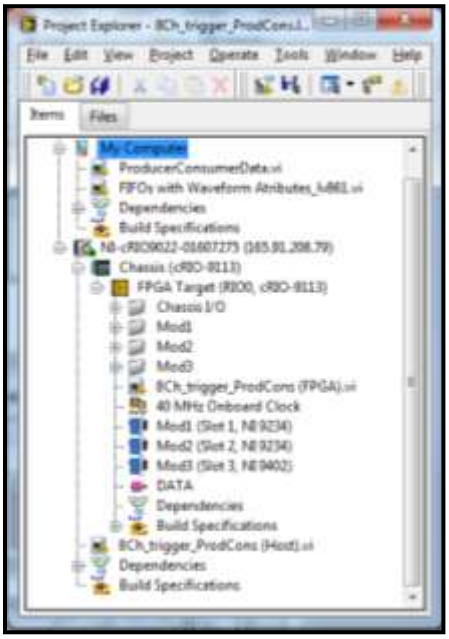

Figure A.15. Project Explorer showing project.

Step 5: Right click on "Build Specifications" at the bottom of the Project Explorer window. Click "create RT Application."

Step 6: To download program to cRIO. Right click on "Build Specifications" again and click "Compile."

A.3. Data collection with UAV platform and cRIO DAQ.

1. Verify all UAV components and DAQ components have been connected. See "Wiring and assembly instructions" section in Appendix B before proceeding.
2. Turn ON the Futaba transmitter.
3. Connect the 2 Sky Lipo 4 cell 4400mAh 14.8V batteries to the Hobbywing ESC. This will allow you to control the control surfaces on the RC plane.
4. Connect the Thunder Power 4 cell 1350mAh 14.8V battery to the Servo-to-Anderson Y-harness to power the cRIO DAQ and microphones. NOTE: DAQ software will "time out" after 90 seconds.
5. Flip Switch A "up" to start collecting microphone information through the cRIO DAQ. Flip Switch A "down" to stop data collection.
6. cRIO software will "shut down" 180 seconds after stopping data collection.

APPENDIX B

B.1. UAV assembly instructions and wiring for flight testing

B.1.1. RC plane components:

1. Hobby Lobby - Sr. Telemaster Plus
    a. Qty: 1
    b. Wingspan: 94”
    c. Fuselage length: 64”
    d. Wing area: 1330 sq. in.
    e. Flying weight: 10 lb. 8 oz.
2. Motrolfly – 8S 310KV Brushless Motor
    a. Qty: 1
    b. Model: DM4325
3. Hobbywing – 100A-HV Brushless Engine Speed Controller (ESC)
    a. Qty: 1
4. Sky LiPo – 4S 14.8V 4400 mAh Lithium Polymer Battery
    a. Qty: 2
5. HiTEC – Standard Servo
    a. Qty: 4;
    b. Model: HS-325HB
6. Futaba – 2.4 GHz Transmitter/Receiver
    a. Qty: 1
    b. Model: T7C

7. Hercules – High Current 5A Battery Eliminator Circuit (BEC)
    a. Qty: 1

B.1.2. DAQ components:

1. National Instrument – cRIO Real-Time Controller
    a. Qty: 1
    b. Model: cRIO – 9022
2. National Instrument – cRIO Reconfigurable Chassis
    a. Qty: 1
    b. Model: cRIO - 9113
3. National Instrument – Analog I/O Module
    a. Qty: 2
    b. Model: NI 9234
4. National Instrument – Digital I/O Module
    a. Qty: 1
    b. Model: NI 9402
5. PUI Audio – Condenser Microphone
    a. Qty: 8
    b. Model: ROM-2238P-NF-R

    NOTE: The 8 microphones are already attached to fuselage. 7 microphones are attached on the outside surface of the UAV. 1 microphone is behind the engine mount.

6. Radio Design Labs – Dual Mic Phantom Adapter
    a. Qty: 4
    b. Model: ST-MPA2
7. Thunder Power – 4S 14.8V 1350 mAh Lithium Polymer Battery
    a. Qty: 1

B.1.3. Wiring and assembly instructions:

1. If the Sr. Telemaster Plus is disassembled, follow instructions inside the Telemaster's box to assemble the UAV. Complete Step 1 before proceeding to Step 2. (Fig. B.1)
2. Screw Hobbywing ESC to nose of plan. (Fig. B.2)
3. Screw the balsa wood engine mount to the noise of the fuselage.
4. Screw the Motrolfly motor to the engine mount and connect to the ESC. (Fig. B.3)
5. Connect micro-plug connector on the ESC to the micro-plug connector on the Hercules BEC. (Fig. B.4)
6. Connect one of the male servo connectors, from one of the Y-harnesses on the BEC, to the female servo connector for the GPS data logger. (Fig. B.5)
7. Connect each microphone, attached to the UAV, to a BNC-to-Servo cable and Y-harness. (Fig. B.6)

8. Connect the male servo connectors on the dual mic phantom adaptors to the female servo connectors on the Y-harnesses attached to the UAV microphones. (Fig. B.7)
9. Connect the male servo connector for PWR on the dual mic phantom adaptor the female servo connector on the Servo-to-Anderson Y-harness. (Fig. B.8)
10. Carefully secure the 2 Sky Lipo 4 cell 4400mAh 14.8V batteries and the 1 Thunder Power 4 cell 1350mAh 14.8V battery inside the fuselage with the 2 Velcro straps. (Fig. B.9)
11. Carefully secure the 4 dual mic phantom adaptor, connected in parallel, inside the fuselage with the Velcro strap. (Fig. B.10)

    NOTE: Make sure 10V are read from each channel of the dual phantom mic adaptors when everything is connected. If voltage is below 10V, adjust the potentiometer on each mic adaptor.
12. Screw the cRIO DAQ to the UAV's cargo door and slide DAQ into the fuselage through the belly of the plane. Use the 3 cargo screws to secure the cRIO DAQ. Also, use the Velcro strip on the cRIO DAQ to tie around the wing's cross-member inside the fuselage. (Fig B.11)
13. Connect the male servo cable to the cRIO DAQ's power terminals. Then connect the male servo cable to the Servo-to-Anderson Y-harness. (Fig. B.12)
14. After cRIO is secured inside the fuselage, connect the BNC connections for mic 1-4 to the first NI 9234 module, closest to the cRIO controller. Connect mic 5-8

to the second NI 9234 module. Connect the last BNC cable (from Ch.5 on the receiver) to the first channel on the NI 9402 module. (Fig. B.13)

15. Attach the Futaba receiver to the inside roof of the fuselage with Velcro. Connect each control surface to its corresponding receiver channel as shown below. (Fig. B.14)

    Channel 1: Wing #1 (left)

    Channel 2: Elevators

    Channel 3: Engine

    Channel 4: Rudder

    Channel 5: Switch B (DAQ Trigger)

    Channel 6: Wing #2 (right)

    Channel 7: Flaps

Fig. B.1. Hobby Lobby – Sr. Telemaster Plus RC plane (UAV).

Fig. B.2. Hobbywing ESC mounted to UAV fuselage.

Fig. B.3. Motrolfly brushless motor mounted to UAV fuselage.

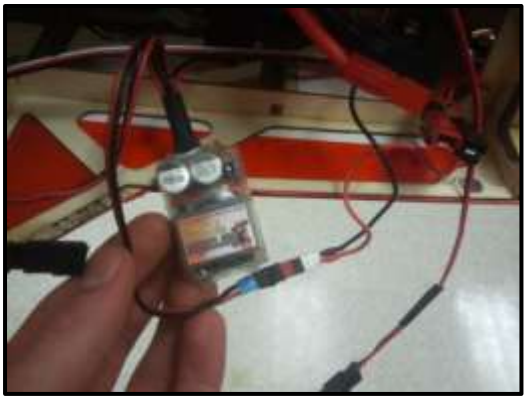

Fig. B.4. Hercules BEC connected to Hobbywing ESC.

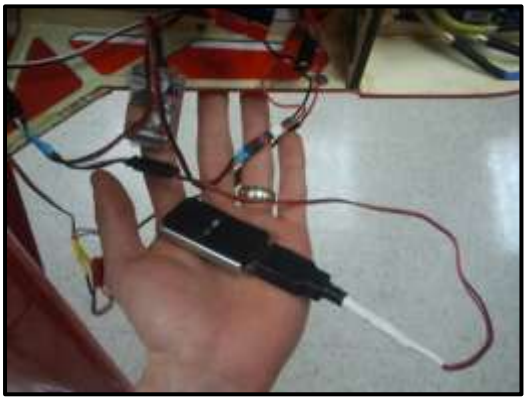

Fig. B.5. GPS data logger connected to BEC.

Fig. B.6. UAV microphone, Y-harness and BNC-to-Servo cable.

Fig. B.7. Dual mic phantom adaptor, UAV microphone, Y-harness and BNC-to-Servo cable.

Fig. B.8. Dual mic phantom adaptor to Servo-to-Anderson Y-harness.

Fig. B.9. The LiPo batteries held secure by Velcro straps.

Fig. B.10. Secure dual mic phantom adaptors inside fuselage via Velcro strap.

Fig. B.11. Insert cRIO DAQ into fuselage.

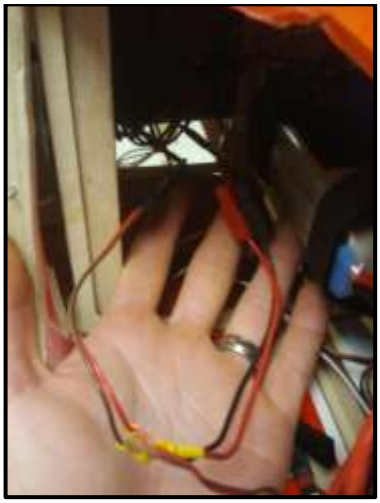

Fig. B.12. Connect cRIO DAQ to Servo-to-Anderson Y-harness.

Fig. B.13. BNC cables connected to corresponding cRIO DAQ channels.

Fig. B.14. Futaba receiver connected to the control surfaces.